

A SUBMILLIMETER PERSPECTIVE ON THE GOODS FIELDS (SUPER GOODS)—I. AN UTRADEEP SCUBA-2 SURVEY OF THE GOODS-N^{1,2,3,4}

L. L. COWIE⁵, A. J. BARGER^{5,6,7}, L.-Y. HSU⁵, CHIAN-CHOU CHEN⁸, F. N. OWEN⁹, W.-H. WANG¹⁰

¹The James Clerk Maxwell Telescope is operated by the East Asian Observatory on behalf of The National Astronomical Observatory of Japan, Academia Sinica Institute of Astronomy and Astrophysics, the Korea Astronomy and Space Science Institute, the National Astronomical Observatories of China and the Chinese Academy of Sciences (Grant No. XDB09000000), with additional funding support from the Science and Technology Facilities Council of the United Kingdom and participating universities in the United Kingdom and Canada.

²The National Radio Astronomy Observatory is a facility of the National Science Foundation operated under cooperative agreement by Associated Universities, Inc.

³The Submillimeter Array is a joint project between the Smithsonian Astrophysical Observatory and the Academia Sinica Institute of Astronomy and Astrophysics and is funded by the Smithsonian Institution and the Academia Sinica.

⁴The W. M. Keck Observatory is operated as a scientific partnership among the the California Institute of Technology, the University of California, and NASA, and was made possible by the generous financial support of the W. M. Keck Foundation.

⁵Institute for Astronomy, University of Hawaii, 2680 Woodlawn Drive, Honolulu, HI 96822, USA

⁶Department of Astronomy, University of Wisconsin-Madison, 475 N. Charter Street, Madison, WI 53706, USA

⁷Department of Physics and Astronomy, University of Hawaii, 2505 Correa Road, Honolulu, HI 96822, USA

⁸Centre for Extragalactic Astronomy, Department of Physics, Durham University, South Road, Durham DH1 3LE, UK

⁹National Radio Astronomy Observatory, P.O. Box O, Socorro, NM 87801, USA

¹⁰Academia Sinica Institute of Astronomy and Astrophysics, P.O. Box 23-141, Taipei 10617, Taiwan

ABSTRACT

In this first paper in the SUPER GOODS series on powerfully star-forming galaxies in the two GOODS fields, we present a deep SCUBA-2 survey of the GOODS-N at both 850 μm and 450 μm (central rms noise of 0.28 mJy and 2.6 mJy, respectively). In the central region the 850 μm observations cover the GOODS-N to near the confusion limit of ~ 1.65 mJy, while over a wider 450 arcmin² region—well complemented by *Herschel* far-infrared imaging—they have a median 4σ limit of 3.5 mJy. We present $\geq 4\sigma$ catalogs of 186 850 μm and 31 450 μm selected sources. We use interferometric observations from the SMA and the VLA to obtain precise positions for 114 SCUBA-2 sources (28 from the SMA, all of which are also VLA sources). We present new spectroscopic redshifts and include all existing spectroscopic or photometric redshifts. We also compare redshifts estimated using the 20 cm to 850 μm and the 250 μm to 850 μm flux ratios. We show that the redshift distribution increases with increasing flux, and we parameterize the dependence. We compute the star formation history and the star formation rate (SFR) density distribution functions in various redshift intervals, finding that they reach a peak at $z = 2 - 3$ before dropping to higher redshifts. We show that the number density per unit volume of $\text{SFR} \gtrsim 500 M_{\odot} \text{ yr}^{-1}$ galaxies measured from the SCUBA-2 sample does not change much relative to that of lower SFR galaxies from UV selected samples over $z = 2 - 5$, suggesting that, apart from changes in the normalization, the shape in the number density as a function of SFR is invariant over this redshift interval.

Keywords: cosmology: observations — galaxies: distances and redshifts — galaxies: evolution — galaxies: starburst

1. INTRODUCTION

The distant, dusty, ultraluminous galaxies first discovered with the Submillimeter Common-User Bolometer Array (SCUBA; Holland et al. 1999) on the 15 m James Clerk Maxwell Telescope (JCMT) (Smail et al. 1997; Barger et al. 1998; Hughes et al. 1998; Eales et al. 1999) are some of the most powerfully star-forming galaxies in the universe (see Casey et al. 2014 for a recent review). Mapping these galaxies is key to understanding how the most massive

galaxies formed and how the shape of the star formation rate (SFR) density distribution function evolves with cosmic time, especially since a significant number of these galaxies are not detected in UV/optical selections. Understanding these galaxies requires wide and deep far-infrared (FIR) and submillimeter surveys with the best possible ancillary data, since such data are essential for determining the redshifts and bolometric luminosities of individual galaxies. In this series of papers, we describe the results of our ultradeep submillimeter survey with the revolutionary SCUBA-2 camera (Holland et al. 2013) on the JCMT of the most heavily studied regions on the sky: the two GOODS fields.

Although ultraluminous infrared galaxies (ULIRGs; $L_{\text{IR}} > 10^{12} L_{\odot}$) contribute only a tiny fraction of the luminosity density in the present-day universe, about 2% at $z = 0.3$ (Le Floc'h et al. 2005), by $z \sim 2$, the high-redshift analogs of ULIRGs—dusty, ultraluminous galaxies with SFRs in excess of $500 M_{\odot} \text{ yr}^{-1}$ that are detected at submillimeter wavelengths—contain a significant fraction of the total star formation out to at least a redshift of 5 (Barger et al. 2000, 2012, 2014; Chapman et al. 2005; Wardlow et al. 2011; Casey et al. 2013; Swinbank et al. 2014). At low redshifts ($z \sim 1$), the evolution of dusty star-forming galaxies can be studied with observations from the *Herschel* satellite alone (e.g., Elbaz et al. 2011; Gruppioni et al. 2013; Magnelli et al. 2013). However, at higher redshifts, the *Herschel* bands that correspond to the peak wavelength in the FIR spectral energy distribution (SED) near $100 \mu\text{m}$ become less sensitive, and by $z \gtrsim 5$, these bands sample wavelengths shorter than the peak wavelength, making longer wavelength observations essential.

At the faintest fluxes, such observations can be obtained from direct Atacama Large Millimeter/submillimeter Array (ALMA) surveys (e.g., Aravena et al. 2016; Bouwens et al. 2016; Fujimoto et al. 2016; González-López et al. 2016; Oteo et al. 2016; Yamaguchi et al. 2016; Dunlop et al. 2017), or by targeting massive cluster lensing fields with single-dish submillimeter telescopes (e.g., Blain et al. 1999; Cowie et al. 2002; Knudsen et al. 2008; Chen et al. 2013a,b; Hsu et al. 2016). However, at brighter fluxes ($\gtrsim 2 \text{ mJy}$ at $850 \mu\text{m}$), the surface density of sources is low, and the small interferometric fields of view and small highly magnified cluster regions make such surveys inefficient. Instead, surveys at these brighter fluxes are best carried out with wide-field imagers on single-dish submillimeter telescopes.

SCUBA-2 is currently the most powerful means to carry out deep, wide-field surveys at submillimeter wavelengths (e.g., Casey et al. 2013; Chen et al. 2013b; Geach et al. 2013, 2017; Barger et al. 2014; Hsu et al. 2016). Many of the highest redshift and most luminous galaxies found in these surveys are not detected in the rest-frame UV/optical, despite extremely deep *HST* observations (e.g., HDF850.1 in the Hubble Deep Field-North (HDF-N), originally detected in the SCUBA map by Hughes et al. 1998; the galaxy’s redshift of $z = 5.18$ was eventually measured from CO observations by Walter et al. 2012). Even when these sources are also detected in the UV/optical, determining their extinction corrections is extremely difficult (e.g., Reddy et al. 2012). Barger et al. (2014) showed that submillimeter selection finds galaxies that are substantially disjoint from UV selection, even when extinction corrections are taken into account. Thus, the dusty, powerfully star-forming galaxy population has to be directly detected and characterized independently of rest-frame UV/optical surveys.

In this first paper in the SUBmillimeter PERspective on the GOODS fields (SUPER GOODS) series, we present our SCUBA-2 observations of the GOODS-N/CANDELS/*Chandra* Deep Field-North (CDF-N). The natural limit of single-dish submillimeter observations is the depth at which confusion becomes important. (This refers to the blending of sources and/or the noise being dominated by unresolved contributions from fainter sources.) For the JCMT, the confusion limit at $850 \mu\text{m}$ is $\sim 1.65 \text{ mJy}$ (see Section 2.1), which corresponds to a SFR of $\sim 220 M_{\odot} \text{ yr}^{-1}$ for a Kroupa (2001) initial mass function (IMF) (see Section 3.1). Since at this flux we can probe the overlap region between submillimeter selected and UV/optical selected galaxy samples, we observed the multiwavelength GOODS-N field to near the confusion limit for a 4σ detection (i.e., an rms level of $\sim 0.4 \text{ mJy}$).

Barger et al. (2014) showed that accurate (subarcsecond) positions for the bulk of the SCUBA-2 sources in the GOODS-N can be found using the deep Karl G. Jansky Very Large Array (VLA) 20 cm (1.4 GHz) observations of F. Owen (2017, in preparation). However, to identify counterparts for sources with ambiguous or missing radio counterparts, we have also obtained submillimeter interferometry with the Submillimeter Array (SMA; Ho et al. 2004). The SMA observations provide accurate positions for 28 of the 186 $850 \mu\text{m}$ SCUBA-2 sources. A further 86 have unique VLA counterparts.

The combination of our uniquely uniform and deep SCUBA-2 map with *Chandra*, *Herschel*, *HST*, *Spitzer*, VLA, and ground-based data provides a rare opportunity to explore in detail the properties of dusty, powerfully star-forming galaxies in the distant universe. (Unfortunately, because of its high northern declination, the GOODS-N cannot be observed with ALMA.) In Section 2, we present our SCUBA-2 data set and its reduction. We describe the identification of multiwavelength counterparts using our VLA and SMA data, and we present the associated redshifts, some of which come from new Keck spectroscopy. We provide $\geq 4\sigma$ $850 \mu\text{m}$ and $450 \mu\text{m}$ catalogs with the counterpart and redshift information, and we compare these source lists with previous work. We also examine how successful the use of

$K_s - 4.5\,\mu\text{m}$ colors is in picking out the galaxies in our $850\,\mu\text{m}$ catalog. In Section 3, we construct SEDs, determine the conversion of submillimeter flux to SFR, and estimate redshifts using $20\,\text{cm}$ to $850\,\mu\text{m}$ and $250\,\mu\text{m}$ to $850\,\mu\text{m}$ flux ratios. We then compute the contributions of the SCUBA-2 sample to cosmic star formation and compare with the total star formation history from the extinction-corrected UV. Finally, we determine the evolution of the SFR density distribution functions with redshift and compare them with those in the UV. In Section 4, we summarize our results. We postpone much of the discussion of the X-ray data to Paper 3 of the series, where we combine the present data with the submillimeter sample for the CDF-S.

We assume the Wilkinson Microwave Anisotropy Probe cosmology of $H_0 = 70.5\,\text{km s}^{-1}\,\text{Mpc}^{-1}$, $\Omega_M = 0.27$, and $\Omega_\Lambda = 0.73$ (Larson et al. 2011).

2. 850 MICRON SOURCES IN THE CDF-N

The depth of multiwavelength coverage on the GOODS-N field makes it one of the best targets for the deepest possible wide-field submillimeter survey. The GOODS-N has a 2 Ms *Chandra* X-ray observation (Alexander et al. 2003), four optical bands (B through z) from the *HST* GOODS-N survey using ACS (Giavalisco et al. 2004), and two near-infrared (NIR) bands from the *HST* CANDELS survey using WFC3 (Koekemoer et al. 2011; Grogin et al. 2011), as well as K_s from Canada-France-Hawaii Telescope (CFHT) observations with WIRCAM (Wang et al. 2010). The *Spitzer* mid-infrared (MIR) observations using MIPS (PI: M. Dickinson) and the *Herschel* FIR observations using PACS and SPIRE (Elbaz et al. 2011; Lutz et al. 2011) are among the deepest ever taken and provide sufficient sensitivity to constrain tightly the thermal SEDs. There is also an ultra-deep $20\,\text{cm}$ image from the upgraded VLA (F. Owen 2017, in preparation). Finally, the field has secure spectroscopic observations for many thousands of galaxies (e.g., Cohen et al. 2000; Wirth et al. 2004, 2015; Cowie et al. 2004, 2016; Barger et al. 2008) and photometric redshifts for many more (e.g., Rafferty et al. 2011). In this section, we present our SCUBA-2 observations and catalogs and some new spectroscopic redshifts of the SCUBA-2 sources that we obtained with the Keck 10 m telescopes. We also describe our use of the impressive ancillary data sets.

2.1. SCUBA-2 Observations

We obtained the data from early 2012 through to mid-2016 using the SCUBA-2 camera. We centered all of the observations on the aimpoint of the *Chandra* X-ray observations at right ascension 12:36:49.6, declination 62:13:53.0 (J2000.0) (Alexander et al. 2003). In the central region, we used the CV DAISY scan pattern to obtain the maximum depth. The CV DAISY field size ($5'5''$ radius; out to this radius the noise is less than twice the central value) is well matched to the deepest portion of the X-ray image. To cover the outer regions to find brighter but rarer sources, we used the PONG-900 scan pattern ($10'5''$ radius; by this radius the noise is twice the central value). Detailed information about the SCUBA-2 scan patterns can be found in Holland et al. (2013).

Table 1. SCUBA-2 Observations

Field	R.A. (J2000.0)	Decl. (J2000.0)	Weather Band	Scan Type	Exposure (Hrs)
CDF-N	12:36:49.6	62:13:53.0	1	CV DAISY	19.8
			2	CV DAISY	25.0
			3	CV DAISY	4.5
			1	PONG-900	14.0
			2	PONG-900	42.0
			3	PONG-900	23.3

We summarize the details of our observations in Table 1, where we give the exposure times and weather conditions (band 1, $\tau_{225\,\text{GHz}} < 0.05$; band 2, $0.05 < \tau_{225\,\text{GHz}} < 0.08$; band 3, $0.08 < \tau_{225\,\text{GHz}} < 0.12$) for each of the scanning patterns observed¹. If we exclude the poorer weather band 3 observations, then we obtained 101 hours on the field,

¹ The program IDs are M12AH15B, M13AH24A, M13BH16B, M14AH22B, M14BH03, M15AH04, M15BH03B, M16AH07B.

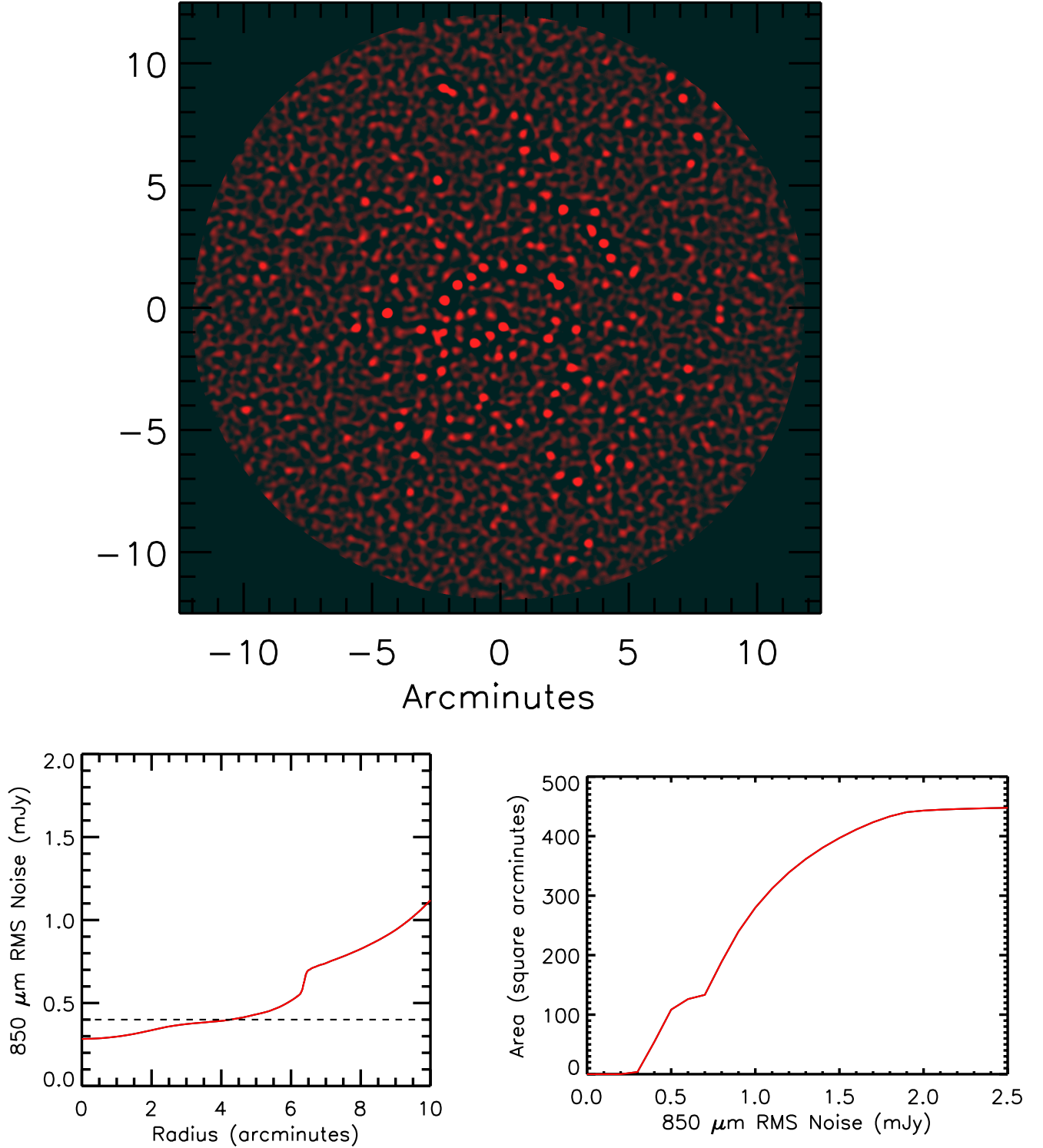


Figure 1. (a) 850 μm matched-filter S/N image. The area of the image is 450 arcmin². (b) Azimuthally averaged 850 μm rms noise vs. radius. The more sensitive central region (radius less than 6') is dominated by the CV DAISY observations, while the outer region is covered by the PONG-900 observations. The black dashed line shows the rms noise corresponding to a 4σ detection threshold of 1.6 mJy, the approximate confusion limit for the JCMT at 850 μm . In (a), the surface density of sources is higher in the central low S/N region of the image. (c) Cumulative area covered vs. 850 μm rms noise.

roughly equally divided between the two scanning modes. While SCUBA-2 obtains simultaneous 450 μm and 850 μm observations, the predominantly band 2 weather implies that the 450 μm observations are not extremely deep, and we focus primarily on the 850 μm data.

Our reduction procedures follow those described in Chen et al. (2013b). We reduced the data using the Dynamic Iterative Map Maker (DIMM) (Jenness et al. 2011; Chapin et al. 2013). DIMM performs iterative estimations on the common mode signal, the astronomical signal, and the white noise. It also applies flat-field and extinction corrections and uses a Fourier Transform filter to remove low-frequency excess signal relative to the white noise that is not able to be removed through common mode subtraction (Chapin et al. 2013). We used the standard configuration faint source file *dimconfig_blank_field.lis*. We ran DIMM on each bolometer subarray individually to avoid data splitting, and we used the MOSAIC_JCMT_IMAGES recipe in the Pipeline for Combining and Analyzing Reduced Data (PICARD; Jenness et al. 2008) to form the final images and noise maps.

We expect nearly all the galaxies to be much smaller than the $\sim 14''$ resolution of the JCMT at 850 μm and hence to appear as unresolved sources. We therefore applied a matched-filter to our maps, which provides a maximum likelihood estimate of the source strength (e.g., Serjeant et al. 2003). Assuming $S(i, j)$ and $\sigma(i, j)$ are the signal and r.m.s noise maps produced by DIMM and $PSF(i, j)$ is the signal point spread function, then the filtered signal map $F(i, j)$ is given by

$$F(i, j) = \frac{\sum_{i,j} [S(i, j)/\sigma(i, j)^2 \times PSF(i, j)]}{\sum_{i,j} [1/\sigma(i, j)^2 \times PSF(i, j)^2]}, \quad (1)$$

and the filtered noise map $N(i, j)$ is given by

$$N(i, j) = \frac{1}{\sqrt{\sum_{i,j} [1/\sigma(i, j)^2 \times PSF(i, j)^2]}}. \quad (2)$$

Ideally, the PSF for the matched-filter algorithm is a Gaussian normalized to a peak of unity with FWHM equal to the JCMT beam size at a given wavelength (i.e., $7''.5$ at 450 μm and $14''$ at 850 μm). However, the map produced from DIMM has low spatial frequency structures that need to be removed. Thus, before running the matched-filter, we convolved the map with a broad Gaussian normalized to a sum of unity, and we subtracted this convolved map from the original map. Chen et al. (2013b) showed that the source fluxes and the signal-to-noise ratio (S/N) are not sensitive to the size of the FWHM for reasonable choices. We adopted values of $20''$ at 450 μm and $30''$ at 850 μm . The PSF used for the matched-filter must be processed in the same way, which results in a Mexican hat-like wavelet with the central Gaussian surrounded by a negative trough.

We calibrated the fluxes using standard Flux Conversion Factors (FCFs; 491 Jy pW $^{-1}$ for 450 μm and 537 Jy pW $^{-1}$ for 850 μm). We applied 10% upward corrections to compensate for the flux lost during filtering (Chen et al. 2013b). We find that the flux calibrations (Dempsey et al. 2013) are accurate to better than 10% based on the variation in the calibrators and the comparison with the SMA data.

In Figure 1(a), we show the 850 μm image made from all of the observations, including the band 3 data. In Figure 1(b), we show the rms noise as a function of the offset angle from the centroid position. In Figure 1(c), we show the cumulative area observed below a given rms noise. For the 450 μm image, we only used the band 1 and band 2 data. We show this image in Figure 2(a). In Figure 2(b), we show rms noise as a function of the offset angle from the centroid position. In Figure 2(c), we show the cumulative area observed below a given rms noise.

Following Chen et al. (2013b), we generated the source catalogs by identifying the peak S/N pixel, subtracting this peak pixel and its surrounding areas using the PSF scaled and centered on the value and position of that pixel, and then searching for the next S/N peak. We iterated this process until we reached a S/N of 3.5. We then limited the sample to the sources with S/N above four. There are 186 detected sources at 850 μm , of which 154 have fluxes above 2 mJy. We present the SCUBA-2 catalogs in Section 2.8; the 850 μm sample can be found in Table 5.

Given the number of resolution elements ($\sim 10^4$) in the SCUBA-2 image, a normal distribution would give ~ 0.3 false sources at the 4σ level. In order to address systematic effects, we also analyzed the negative of the image. To remove the negative troughs produced in the processing, we first cleaned the image of all the positively detected sources. We then searched for sources in the negative of the image, finding four sources with fluxes above 2 mJy and S/N above 4. This may be compared with the 156 sources detected in the positive image with the same thresholds.

The central regions of the 850 μm image have very low noise, and confusion effects may become significant (e.g., Condon 1992). (Confusion may be safely ignored in the 450 μm image, which is higher resolution and shallower.) There are two types of confusion: the first is blending, which is usually considered to become important when there is more than one source per 30 beams, and the second is noise from sources below the flux limit of interest, which we

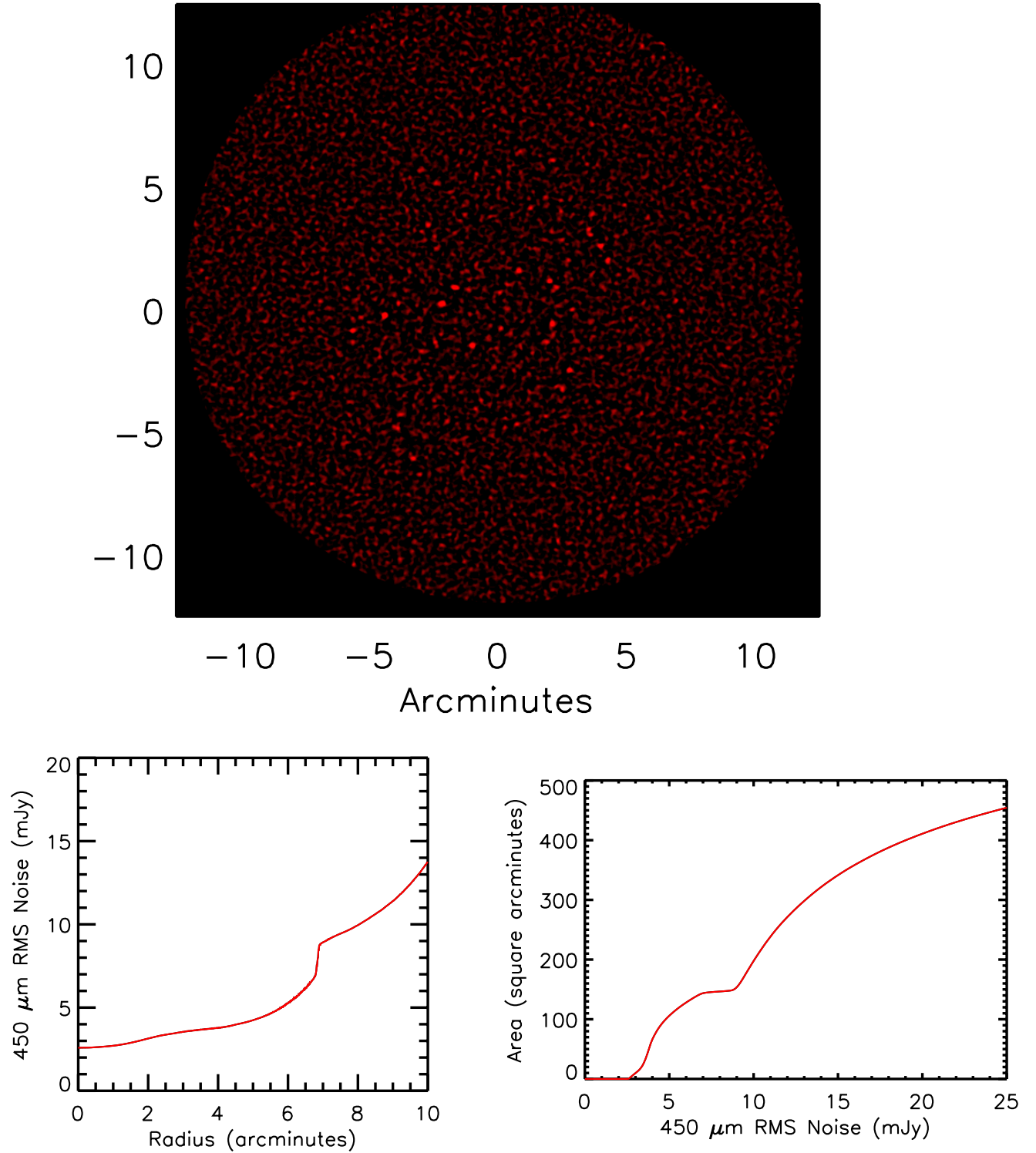


Figure 2. (a) 450 μm matched-filter S/N image. Only the central region covered by the CV DAISY scans is shown, since the noise outside this region is high. All but one of the $\geq 4\sigma$ sources (white points) lie within this region. (b) Azimuthally averaged 450 μm rms noise vs. radius. The more sensitive central region (radius less than 6') is dominated by the CV DAISY observations, while the outer region is covered by the PONG-900 observations. (c) Cumulative area covered vs. 450 μm rms noise.

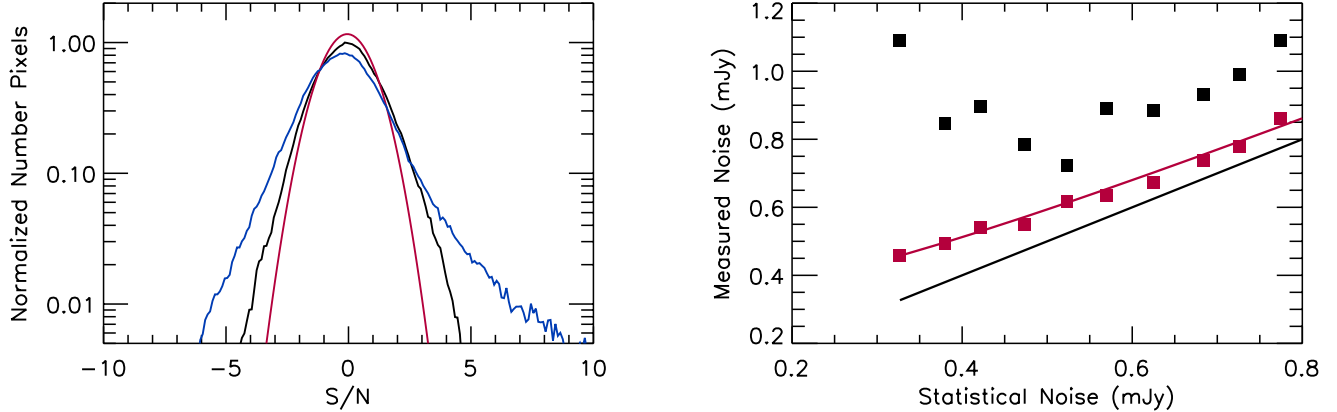


Figure 3. (a) Distribution of S/N from pixel to pixel in the central (low noise) region of the image where the $850\,\mu\text{m}$ rms noise is less than $0.6\,\text{mJy}$. The blue curve shows the distribution for the raw image, while the black curve shows the distribution when all sources brighter than $2\,\text{mJy}$ are removed. The red curve shows the expected distribution from the statistical noise. (b) Measured $850\,\mu\text{m}$ rms noise in circular annuli vs. mean statistical noise. The black squares show the values measured in the raw image. The red squares the values measured in the image after the sources brighter than $2\,\text{mJy}$ are removed. The black curve shows the expectation from the statistical noise, and the red curve the result when a confusion noise of $\sigma_c = 0.32\,\text{mJy}$ is added in quadrature.

call σ_c . The total noise is the combination of the noise measured from the SCUBA-2 signal, which we refer to as the statistical noise, σ_s , and σ_c ; it is given by $\sigma = (\sigma_s^2 + \sigma_c^2)^{0.5}$.

We can estimate both the blending limit and σ_c from the fits to the $850\,\mu\text{m}$ counts of Hsu et al. (2016). Based on the counts, we find more than one source per 30 beams below $1.64\,\text{mJy}$, which is a lower flux than that of any of the sources in the present sample. Thus, blending is not that important for our sample. In order to estimate σ_c , we simulated an image using the counts and the PSF of the matched-filter image and then measured the dispersion in the simulated image. We found $\sigma_c = 0.33\,\text{mJy}$ for sources with fluxes less than $2\,\text{mJy}$. The value of σ_c is not sensitive to the low flux cutoff, which we took as $0.005\,\text{mJy}$.

We can also estimate σ_c directly from the image by comparing the measured dispersion with the statistical noise. As the statistical noise becomes smaller, we expect to see the measured noise rise above it and reach a constant value equal to σ_c . In Figure 3(a), using only the portion of the image with noise less than $0.6\,\text{mJy}$, we show the distribution of the actual S/N relative to the statistical noise for both the raw matched-filter image (blue curve) and the matched-filter image with the sources brighter than $2\,\text{mJy}$ removed (black curve). The red curve shows the expectation from the statistical noise alone. The figure emphasizes the importance of removing the brighter sources, which otherwise would dominate the noise, but even with these removed, the black curve is wider than the red curve due to the confusion noise. In Figure 3(b), we show the comparison of the measured noise in radial annuli (the statistical noise increases with radius) versus the mean statistical noise in each annulus. The black squares show the values measured from the matched-filter image, and the red squares the values measured from the matched-filter image with the sources brighter than $2\,\text{mJy}$ removed. The black squares have a median value of $\sim 0.89\,\text{mJy}$ for the points with statistical noise less than $0.6\,\text{mJy}$, which is very similar to that measured by Geach et al. (2017) for the same quantity. This noise is dominated by the brighter sources and shows significant variation due to the small number statistics of these sources. In order to measure σ_c from the faint sources only, we use the measured noise with the bright sources removed. We can compare this with the statistical noise (black curve) to estimate the σ_c from sources fainter than $2\,\text{mJy}$. The red curve shows the result of adding $\sigma_c = 0.33$ in quadrature to the statistical noise; it gives a good approximation to the values measured from the image with the sources brighter than $2\,\text{mJy}$ removed. This value of σ_c is in good agreement with the value that we estimated from the counts and is comparable to the minimum statistical noise in the image. Thus, we conclude that we are just reaching the confusion noise limit in the image.

We finally tested the completeness of source recovery in the central region. To do so, we added a small number of sources (usually 5) of a given flux at random positions in the central low noise portion of the image ($< 0.6\,\text{mJy}$). We then ran the finding procedure to obtain the source list including the introduced sources. We considered a source to be recovered if it was within $4''.5$ of the original position and had a flux that was less than 3σ different from its actual value. We repeated the procedure 100 times for each flux. We summarize the results in Table 2 for sources with input

fluxes of 5 mJy, 3 mJy, and 2 mJy, where we give the input flux, the percentage recovered, the mean recovered flux divided by the input flux, and the dispersion of the recovered sources, which we show as the mean statistical noise of the sample together with the additional σ_c required to match the measured dispersion. We omit σ_c from the table for the 2 mJy sources where the dispersion is biased by the omission of the downward scattered sources which are not recovered. The recovery rate is high ($> 90\%$ at 3 mJy), upward boosts are small, and the inferred noise is consistent with our previous estimates of σ_c .

Table 2. Source Recovery

Flux (mJy)	Recovered Fraction	Boost	σ_s (mJy)	σ_c (mJy)
5	0.93	1.01	0.40	0.37
3	0.91	1.01	0.40	0.33
2	0.72	1.11	0.40	...

2.2. SMA Observations

We need interferometric follow-up observations to identify the true optical, NIR, and MIR counterparts to the SCUBA-2 sources. With such data, we can find accurate positions and determine whether a SCUBA-2 source is a blend of emission from multiple galaxies. Such multiples are not uncommon in the brighter submillimeter detected populations (e.g., Wang et al. 2011; Barger et al. 2012; Smolčić et al. 2012; Chen et al. 2013b; Hodge et al. 2013; Karim et al. 2013; Simpson et al. 2015; Miettinen et al. 2015). In Section 2.3, we discuss how most of the SCUBA-2 sources can be identified with ultra-deep VLA 20 cm imaging. However, sometimes there are two or more potential 20 cm counterparts; thus, it is generally best if the positions can be measured from submillimeter interferometry. We observed nearly all of the brighter SCUBA-2 sources with the SMA. Including archival data from other SMA programs, we have identifications for 33 submillimeter sources with the SMA. These correspond to 28 of the SCUBA-2 sources. Because of the sensitivity limits, we did not attempt spectroscopy with the SMA.

We performed the calibration and data inspection using the IDL-based Caltech package MIR modified for the SMA. We generated continuum data by averaging the spectral channels after doing the passband phase calibration. We used both gain calibrators to derive gain curves. For consistency checks, we compared these results with those obtained by adopting just one calibrator. We did not find any systematic differences. We performed the flux calibrations using data taken under conditions (time, hour angle, and elevation) similar to the conditions of the flux calibrator observations. The flux calibration error is typically within $\sim 10\%$ with this method. We exported the calibrated interferometric visibility data to the package MIRIAD for subsequent imaging and analysis. We weighted the visibility data inversely proportional to the system temperature and Fourier transformed them to form images. We also applied the “robust weighting” of Briggs (1995), with a robust parameter of 1.0, to obtain a better balance between beam size and S/N. We CLEANed the images around detected sources to approximately 1.5 times the noise level to remove the effects of the sidelobes. (The results are not sensitive to choosing a slightly deeper CLEANing level, such as 1.0 times the noise.) The upgrade of the SMA to a 4 GHz bandwidth during the course of our observing program considerably improved the continuum sensitivity and made calibrations with fainter quasars easier. We typically achieved rms $\sim 1.2 - 1.5$ mJy in a night with the old 2 GHz bandwidth and rms $\sim 0.7 - 0.9$ mJy in a night with the new 4 GHz bandwidth. All of the SMA fluxes and flux errors that we quote are primary-beam corrected. We measured source positions and fluxes by fitting the images with point-source models using the MIRIAD IMFIT routine.

In Table 3, we provide the identification number (Column 1), the name based on the SMA coordinate (Column 2), the right ascension and declination measured from the SMA image (Columns 3 and 4), the 860 μ m SMA flux and error (Columns 5 and 6), and the S/N (Column 7) for the 33 4σ detected SMA sources. All of the SMA detected sources correspond to 20 cm sources (Section 2.3), and we include the 20 cm fluxes in the table (Column 8). We also include spectroscopic redshifts, where available (Column 9; see Section 2.7). Finally, we give the identification number from Table 5 of the nearest SCUBA-2 850 μ m source (Column 10).

Six of the SMA detected sources (three pairs) are separated by less than the SCUBA-2 FWHM (identification numbers (21, 27), (28, 32), and (29, 31) from Table 3, with the last being an extremely close pair with a $2''$ separation). All of

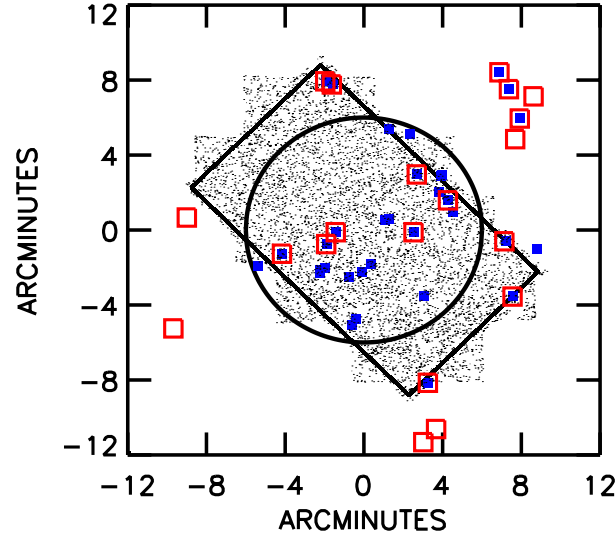


Figure 4. Positions of the 19 4σ SCUBA-2 sources with fluxes > 7 mJy (red open squares) and of the 33 4σ SMA sources (blue squares). The large circle shows a $6'$ radius where the $850\mu\text{m}$ rms noise reaches the confusion limit for the JCMT of 2 mJy (4σ). This is also the deepest portion of the *Chandra* X-ray image. The shading shows the full region of the *HST* GOODS-N imaging, while the rectangle shows the most uniformly covered portion. The GOODS-*Herschel* PACS observations cover roughly the same area as the *HST* GOODS-N observations, while the GOODS-*Herschel* SPIRE observations cover the full SCUBA-2 field.

these sources were identified as multiple contributors to single SCUBA sources in Wang et al. (2011) and Barger et al. (2012). (Note that the (28, 32) pair was considered a triplet with 22 in those papers, but 22 is farther away and now corresponds to SCUBA-2 source 77 in Table 5.) While two of the pairs still correspond to single sources in the present SCUBA-2 data, the (28, 32) pair now corresponds to two separate SCUBA-2 sources, 119 and 102, respectively, in Table 5. Thus, we are left with only two clear multiples in the SCUBA-2 sources with SMA observations.

Table 3. SMA 4σ Sources

No	Name	R.A.	Decl.	Flux	Error	S/N	20cm	z	SCUBA-2
		J2000.0	J2000.0	(mJy)	(mJy)		(μJy)		No.
(1)	(2)	(3)	(4)	(5)	(6)	(7)	(8)	(9)	(10)
1	SMA123711622211	12 37 11.70	62 22 11.9	23.9	2.50	9.5	87	4.055	2
2	SMA123555622239	12 35 55.85	62 22 39.3	17.0	1.90	8.9	56	...	4
3	SMA123730621258	12 37 30.79	62 12 58.9	14.9	0.90	16.5	126	...	3
4	SMA123546622013	12 35 46.65	62 20 13.7	14.0	2.20	6.3	85	...	5
5	SMA123551622147	12 35 51.35	62 21 47.3	13.7	2.80	4.8	51	...	1
6	SMA123633621408	12 36 33.44	62 14 8.69	12.0	1.40	8.5	33	4.042	8
7	SMA123627620605	12 36 27.19	62 06 5.50	11.5	0.70	16.4	34	...	7
8	SMA123550621042	12 35 50.22	62 10 42.4	10.1	2.70	3.7	25	...	12
9	SMA123708622202	12 37 8.825	62 22 2.09	9.2	1.00	9.2	143	4.051	10
10	SMA123634621923	12 36 34.92	62 19 23.7	8.9	2.10	4.2	63	...	20
11	SMA123539621312	12 35 39.49	62 13 12.1	8.5	0.50	17.0	35	...	39
12	SMA123651621225	12 36 51.98	62 12 25.7	7.8	1.00	7.8	12	5.183	26
13	SMA123628621045	12 36 28.84	62 10 45.2	7.7	0.90	8.5	48	...	63
14	SMA123618621550	12 36 18.32	62 15 50.7	7.2	0.70	10.2	163	2.000	18
15	SMA123707621408	12 37 7.210	62 14 8.30	7.1	1.40	5.0	25	2.490	15

Table 3 continued on next page

Table 3 (*continued*)

No	Name	R.A.	Decl.	Flux	Error	S/N	20cm	<i>z</i>	SCUBA-2
		J2000.0	J2000.0	(mJy)	(mJy)		(μ Jy)		No.
(1)	(2)	(3)	(4)	(5)	(6)	(7)	(8)	(9)	(10)
16	SMA123741621220	12 37 41.14	62 12 20.4	7.1	1.80	3.9	27	...	35
17	SMA123631621714	12 36 31.92	62 17 14.7	7.1	0.50	14.2	21	...	14
18	SMA123711621331	12 37 11.31	62 13 31.1	6.7	0.60	11.1	123	1.995	13
19	SMA123644621937	12 36 44.08	62 19 37.9	6.4	1.10	5.8	25	...	24
20	SMA123622621616	12 36 22.08	62 16 16.2	5.4	0.60	9.0	26	...	42
21	SMA123643621450	12 36 43.97	62 14 50.7	5.3	1.10	4.8	30	2.095	31
22	SMA123712621212	12 37 12.00	62 12 12.2	5.3	0.90	5.8	33	2.914	77
23	SMA123701621145	12 37 1.600	62 11 45.9	4.8	0.60	8.0	95	1.760	25
24	SMA123658620931	12 36 58.53	62 09 31.6	4.6	0.60	7.6	27	...	65
25	SMA123655621201	12 36 55.92	62 12 1.91	4.5	0.80	5.6	25	2.737	80
26	SMA123553621337	12 35 53.23	62 13 37.9	4.3	0.80	5.3	41	2.098	19
27	SMA123646621448	12 36 46.09	62 14 48.5	4.2	0.80	5.2	101	...	31
28	SMA123714621208	12 37 14.26	62 12 8.10	4.1	0.70	5.8	25	3.157	119
29	SMA123621621708	12 36 21.29	62 17 8.08	3.5	0.70	5.0	164	...	51
30	SMA123616621513	12 36 16.10	62 15 13.7	3.4	0.60	5.6	36	2.578	43
31	SMA123621621709	12 36 21.10	62 17 9.59	3.4	0.60	5.6	44	1.992	51
32	SMA123714621156	12 37 14.03	62 11 56.4	3.2	0.90	3.5	22	...	102
33	SMA123700620909	12 37 0.300	62 09 9.89	3.1	0.60	5.1	297	...	112

In Figure 4, we compare the positions of the SMA detected sources (blue squares) with those of the brighter SCUBA-2 sources (red open squares). For the latter, we only show fluxes greater than 7 mJy that would be detected above the 4σ level throughout the entire 450 arcmin² field. All of the bright SCUBA-2 sources in the deep portion of the CDF-N (large circle) and the *HST* GOODS-N region (shading) have SMA detections.

Since the measured SMA and SCUBA-2 fluxes are independent, we can use them to check the flux calibration. In Figure 5, we plot SCUBA-2 850 μ m flux versus SMA flux. The SCUBA-2 fluxes are 8% lower than the SMA fluxes, which is within the systematic error in the calibration. The point with the higher SMA flux than SCUBA-2 flux is GN20 (Pope et al. 2005), where the measured SMA flux is from Younger et al. (2008). Younger et al. measured GN20 in the extended configuration of the SMA; thus, the correction to a total flux is somewhat uncertain. The remaining sources were observed in the compact mode of the SMA where the spatial resolution is 2'' at 345 GHz. We do not expect these sources to be resolved, and the measured SMA flux should be a good approximation to the total flux.

2.3. VLA 20 cm Observations

The upgrade of the VLA has greatly increased the sensitivity of the decimetric continuum observations that can be obtained, making it possible to identify radio counterparts to nearly all of the brighter SCUBA-2 sources. Here we use the extremely deep 20 cm image of the CDF-N reduced by F. Owen (2017, in preparation). The image covers a 40' diameter region with an effective resolution of 1''8. The absolute radio positions are known to 0''.1 – 0''.2 rms. The highest sensitivity region, about 9' in radius, is closely matched to the full area of the present SCUBA-2 survey and completely covers the deepest region, providing a relatively uniform 20 cm rms of 2.3 μ Jy for determining the radio fluxes of the SCUBA-2 sources. There are 787 distinct $\geq 5\sigma$ radio sources within the 9' radius, excluding sources that appear to be parts of other sources.

We first inspected each of the SCUBA-2 sources to determine possible radio counterparts. In Figure 6, we show images of each of the SCUBA-2 sources with fluxes above 2 mJy (right thumbnails) ordered by increasing 850 μ m flux (see Table 5) starting from the bottom left of the figure, along with the corresponding radio images (left thumbnails). In the left thumbnails, we mark the sources from the $\geq 5\sigma$ radio catalog with small circles and any SMA detections

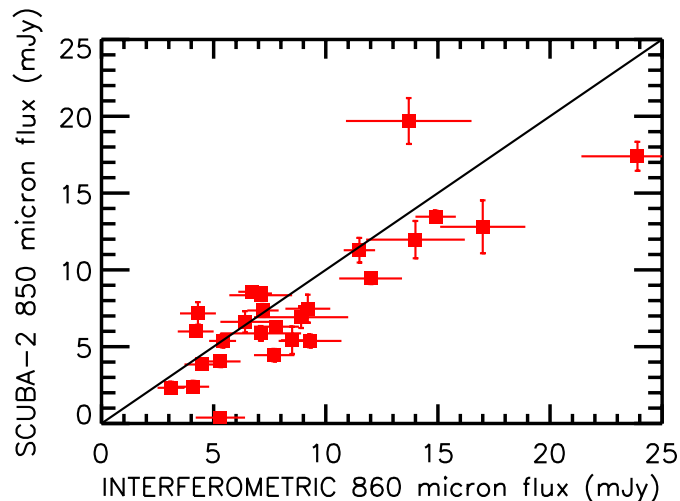


Figure 5. SCUBA-2 flux vs. SMA flux (red squares). Only SCUBA-2 sources with a single counterpart in the SMA field are shown to avoid SCUBA-2 sources with multiple contributing galaxies. The SCUBA-2 fluxes are measured at the nominal positions of the SMA sources, which provide the most accurate positions in the SCUBA-2 image. Error bars are 1σ in each axis.

with larger circles. As discussed in Section 2.2 and shown in Table 3, all of the SMA detections correspond to a radio source.

When an SMA detection determines the radio counterpart, or when there is a single radio source within a $4''.5$ search radius from the SCUBA-2 position, then we consider the SCUBA-2 source to have a unique counterpart identification, and we adopt the radio position as the accurate position for the SCUBA-2 source. This localizes 114 of the 186 sources, including 26 of the 29 sources with $850\mu\text{m}$ fluxes above 6 mJy. Many of the remaining SCUBA-2 sources have multiple potential radio counterparts and no SMA follow-up observation to decide on the correct one. (See Figure 7, where we show the four such sources with $850\mu\text{m}$ fluxes above 4 mJy.) However, 39 of the 154 $850\mu\text{m}$ SCUBA-2 sources with fluxes greater than 2 mJy have no potential radio counterparts within our match radius. These are primarily drawn from the faintest SCUBA-2 sources; the brightest source without a radio counterpart has a flux of 6.67 mJy (source 23 in Table 5 and Figure 6).

The present radio identification rate (more than 75% for sources with $850\mu\text{m}$ flux > 2 mJy) represents a substantial improvement over previous radio matches, which typically yielded 60–70% matching for sources with $850\mu\text{m}$ fluxes > 5 –8 mJy (e.g., Barger et al. 2000; Ivison et al. 2002; Chapman et al. 2003). In Figure 8, we illustrate the gain in counterpart matching as a function of the 20 cm rms.

The radio blank sources are of particular interest as being potentially at high redshift. The highest redshift sources in the sample with known spectroscopic redshifts $z > 3$ (blue circles in Figure 8) have low radio fluxes relative to their submillimeter fluxes (Carilli & Yun 1999; Barger et al. 2000), reflecting the opposing K -corrections in the radio and submillimeter.

We may use the offsets of the counterparts relative to the SCUBA-2 $850\mu\text{m}$ centroid positions to estimate the accuracy of the SCUBA-2 positions and to justify our choice of a $4''.5$ matching radius. We first checked the absolute astrometric pointing of the SCUBA-2 observations. Comparing with the SMA detected sources, we find an absolute offset of $0''.75$ in right ascension and $0''.4$ in declination. Comparing with the VLA detected sources, we find $0''.5$ in right ascension and $0''.3$ in declination. Both offsets are small compared with the positional uncertainties in the SCUBA-2 sources. In Figure 9, we show the offsets of the individual SMA (red) and radio (black cross-hatching) counterparts. The mean offsets are $1''.4$ for the (on average, brighter) sample with SMA counterparts and $1''.9$ for the larger and fainter sample with radio counterparts. Nearly all of the SMA counterparts lie within $3''.5$ of the SCUBA-2 position, and 96% of the radio counterparts lie within $4''$. This positional uncertainty emphasizes the difficulty of working directly with the SCUBA-2 positions. In our analysis, we will focus on the SCUBA-2 sources with unique counterparts and accurate positions. However, it should be noted that most of the very high S/N SCUBA-2 sources do have fairly accurate positions from the SCUBA-2 data alone. For example, for the SCUBA-2 sources with $S/N > 10$, the mean offset from the SMA or radio counterparts is $1''.2$, while at $S/N > 6$, it is $1''.7$.

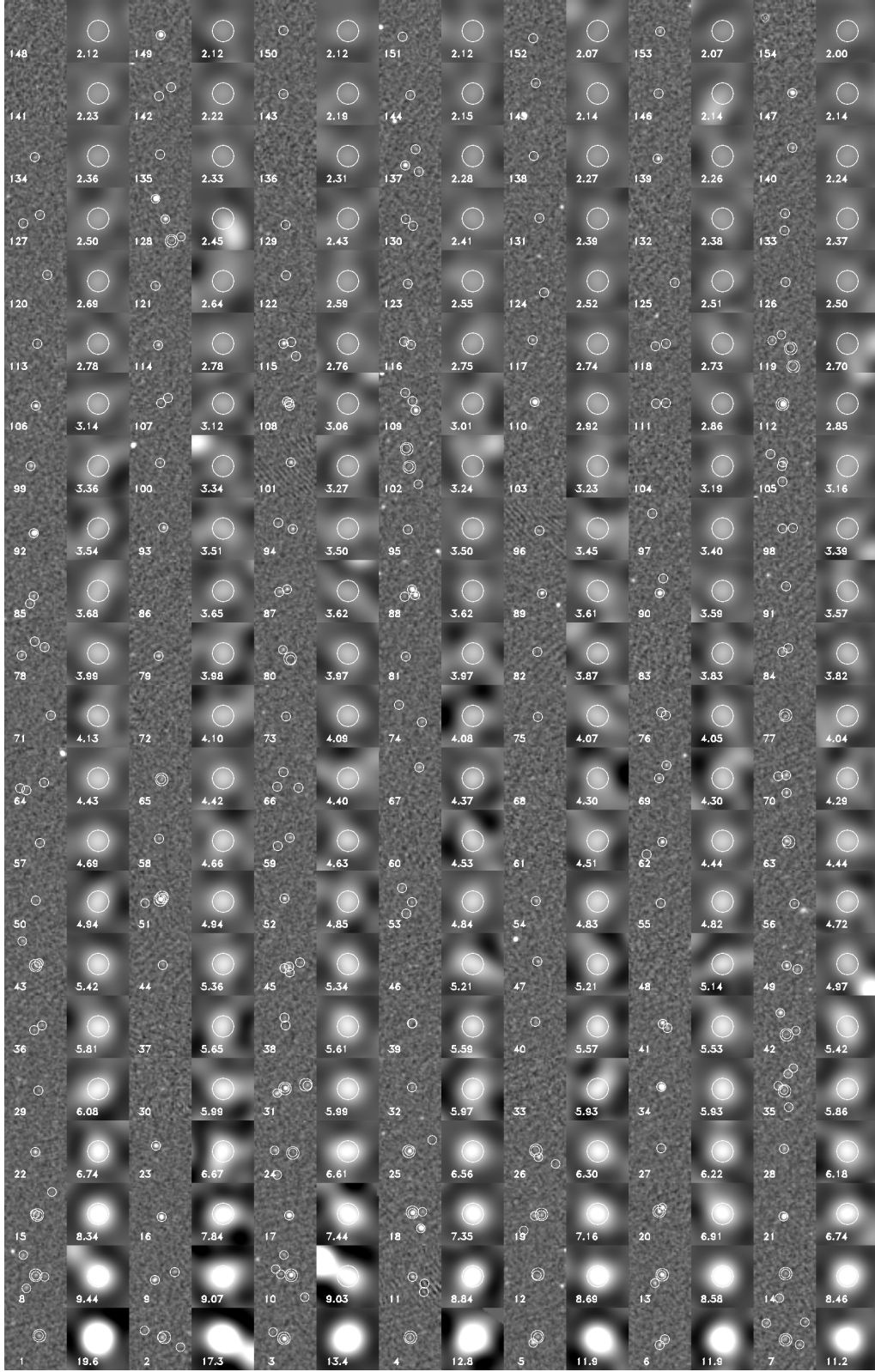


Figure 6. Thumbnails ($40''$ on a side) of the $\geq 4\sigma$ SCUBA-2 sources with $850\mu\text{m}$ fluxes above 2mJy . In each case, we show the radio image in the left thumbnail and the SCUBA-2 image in the right thumbnail. In the left thumbnails, the small circles show the positions of the $\geq 5\sigma$ 20cm sources, while the larger circles show the positions of the SMA detections. In the right thumbnails, the large circle shows the $14''$ diameter beam width. The thumbnails (source number given at the bottom of the left thumbnails) are shown in order of decreasing $850\mu\text{m}$ flux (flux given at the bottom of the right thumbnails), starting from the bottom left of the figure.

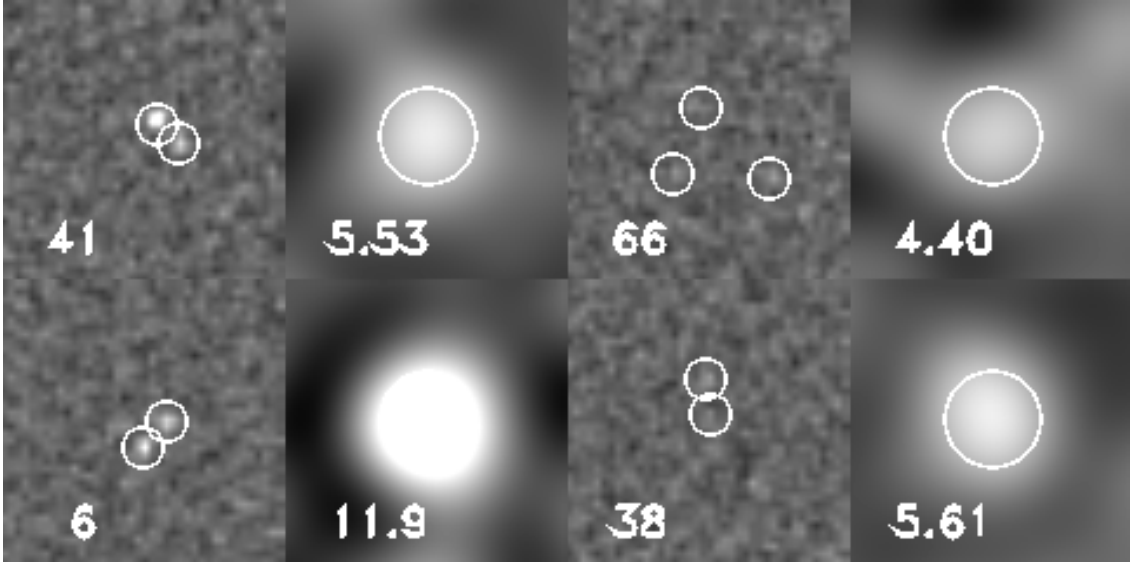


Figure 7. Blow-ups of the thumbnails in Figure 6 corresponding to the four sources with $850\,\mu\text{m}$ fluxes above 4 mJy that have multiple radio counterparts but no SMA follow-up observations. In each case, we show the radio image in the left thumbnail and the SCUBA-2 image in the right thumbnail. In the left thumbnails, the small circles show the positions of the $\geq 5\sigma$ 20 cm sources. In the right thumbnails, the large circle shows the $14''$ diameter beam width. The thumbnails (source number given at the bottom of the left thumbnails) are shown in order of decreasing $850\,\mu\text{m}$ flux (flux given at the bottom of the right thumbnails), starting from the bottom left of the figure.

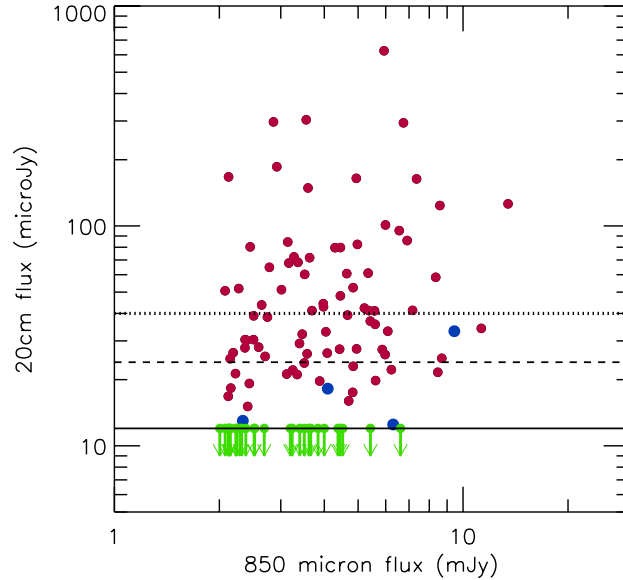


Figure 8. Radio counterparts to the $\geq 4\sigma$ SCUBA-2 sources with $850\,\mu\text{m}$ fluxes above 2 mJy and lying within the $9'$ highest sensitivity region of the radio image (red circles—sources with an SMA identification, or where there is a single radio counterpart within $4''.5$ of the SCUBA-2 position; green circles with downward pointing arrows—sources where there is no radio counterpart within the $4''.5$ search radius; blue circles—sources where there is a spectroscopic redshift $z > 3$). The horizontal lines show the 5σ limits of the F. Owen (2017, in preparation) (solid), Morrison et al. (2010) (dashed), and Richards et al. (2000) (dotted) 20 cm observations.

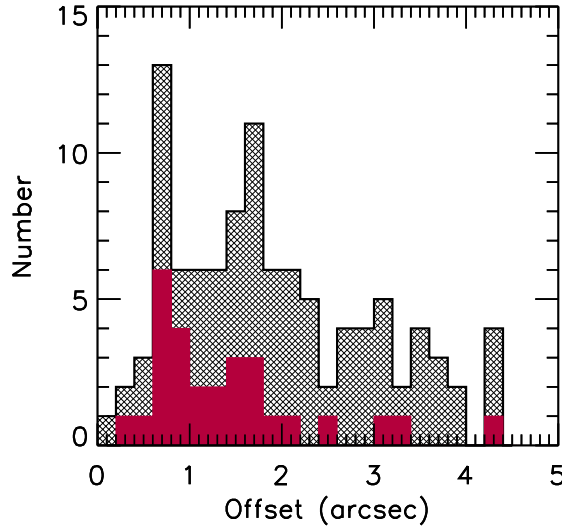


Figure 9. Offsets from the SCUBA-2 850 μm centroid positions of the individual radio (black cross-hatching; the mean offset is 1.9) and SMA (red; the mean offset is 1.4 for these higher flux 850 μm sources) counterparts.

2.4. Optical and NIR Counterparts

Of the 102 SCUBA-2 sources with accurate positions (i.e., with SMA measurements and/or single VLA counterparts) and 850 μm fluxes above 2 mJy (there are 114 total with accurate positions; see Section 2.3), 57 lie in the most uniformly covered portion of the *HST* GOODS-N (rectangle in Figure 4). Of these, 43 have magnitudes from the *HST* GOODS-N catalog (Giavalisco et al. 2004; we use the auto magnitudes) using a 1.5 matching radius. In the NIR, we use similarly measured auto magnitudes from the *HST* CANDELS data (Grogin et al. 2011; Koekemoer et al. 2011). The CFHT WIRCAM K_s image from Wang et al. (2010) covers the full SCUBA-2 field, so we also use corrected 3" diameter aperture magnitudes from this image (102 sources; see Table 5).

All of the sources with fluxes above 6 mJy in the *HST* GOODS-N have SMA detections and precise positions. In Figure 10, we show three-color thumbnails for these 12 sources, with blue representing F450W (*B*-band), green F814W (*I*-band), and red F160W (*H*-band). The positions of the SCUBA-2 sources are marked by the SMA centroids (white squares) and the VLA radio contours (white). If there is a spectroscopic redshift (CO or optical/NIR; see Section 2.7), then it is given in the upper left of the thumbnail image next to the identification number from Table 5. The images show the very dusty nature of the galaxies. The lower redshift galaxies are usually only visible in the NIR band, and the higher redshift galaxies are often absent in all the bands. Where emission is seen in the higher redshift galaxies, it generally lies outside the *high surface brightness regions in the submillimeter and radio images*. For example, in the sources with identification numbers 2 and 10, known as GN20 and GN20.2 (Pope et al. 2005), respectively, the green blobs show material at the redshift of the galaxy but lying outside the bright radio emission (Hodge et al. 2015). The heavy levels of extinction make determining morphologies extremely difficult, and only one of the SCUBA-2 galaxies shown in Figure 10 (identification number 13) appears to be a clear merger based on both the NIR and radio morphologies. The sources with identification numbers 3 and 18 could perhaps be fainter mergers.

2.5. IRAC Fluxes

We used the catalog of Wang et al. (2010) to obtain the IRAC fluxes. Wang et al. used K_s priors to deblend sources in the IRAC 3.6 μm , 4.5 μm , 5.6 μm , and 8.0 μm images obtained from the *Spitzer* GOODS Legacy program (PI: M. Dickinson). Wang et al. (2010) also included sources without K_s counterparts in their final catalog. Of the 102 SCUBA-2 sources with accurate positions and 850 μm fluxes above 2 mJy (there are 114 total with accurate positions; see Section 2.3), 71 lie within the deep IRAC area covered by the Wang et al. catalog. Of these, 68 have 4.5 μm counterparts within a 1.5 matching radius. The remaining 3 sources each lie too close to a very bright neighbor for accurate measurements.

In Figure 11, we show the distributions of (a) the 4.5 μm magnitudes (68 sources) and (b) the K_s magnitudes (102 sources). The distribution of the 4.5 μm magnitudes is considerably brighter than that of the K_s magnitudes, with all but three of the detected sources having a 4.5 μm magnitude brighter than 23. This reflects the well-known result that bright submillimeter detected galaxies are very red at these wavelengths. Indeed, Wang et al. (2012) developed a

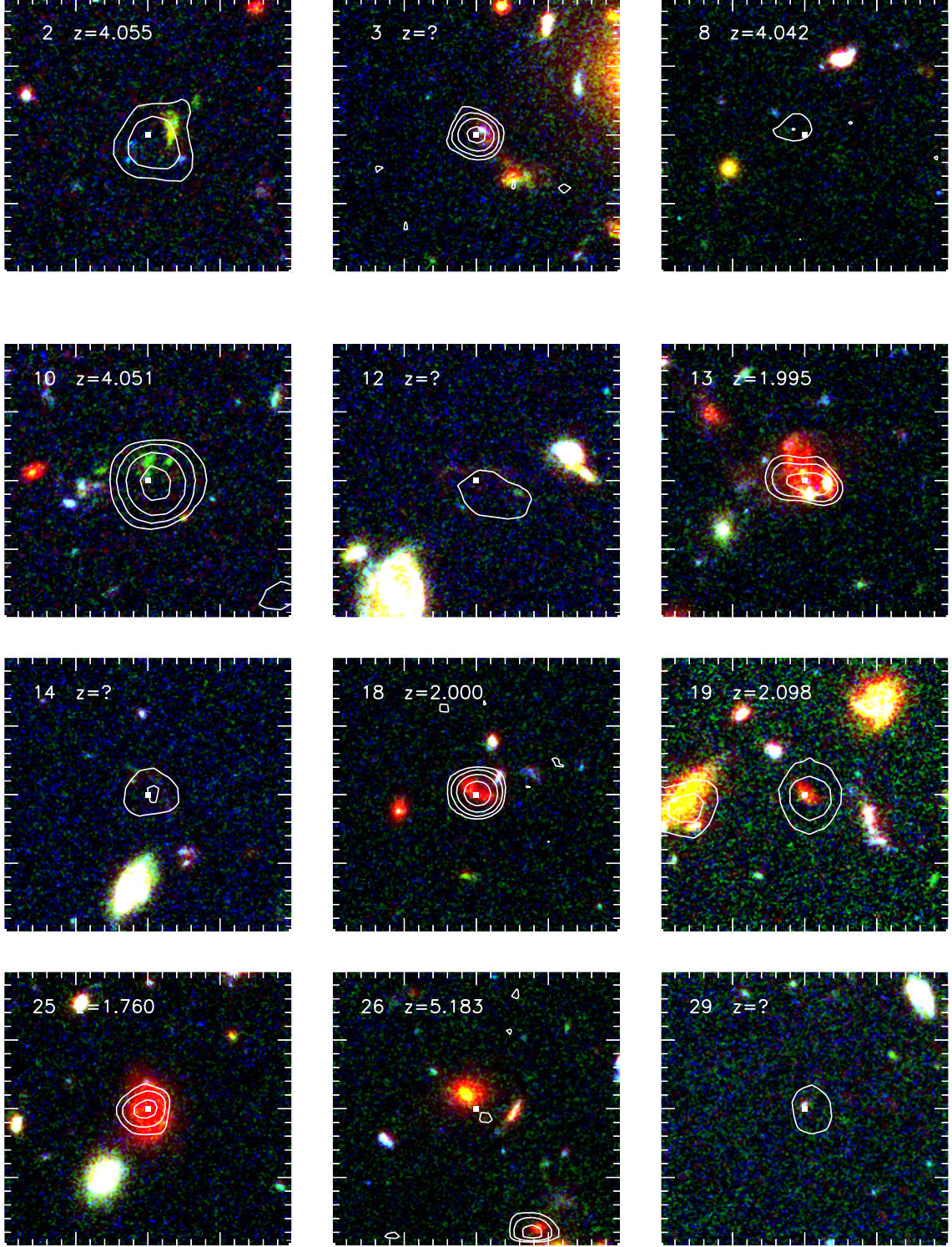


Figure 10. Three-color (F450W, F814W, and F160W) *HST* images of the 12 brightest SCUBA-2 sources in the *HST* GOODS-N region. The thumbnails are $10''$ on a side. In each case, the white square marks the centroid from the SMA observation, and the white contours are from the VLA 20 cm observation. The identification numbers refer to Table 5, and the redshifts are spectroscopic (either optical/NIR or CO). The sources with identification numbers 2, 10, and 26 are the well-known galaxies GN20, GN20.2, and HDF850.1, respectively.

method that uses red $K_s - 4.5 \mu\text{m} > 1.6$ colors to select high-redshift, dusty galaxies (called KIEROs). Other groups have similarly used red $H - 4.5 \mu\text{m} > 2.25$ colors (HIEROS; e.g., Caputi et al. 2012; Wang et al. 2016) or red colors in

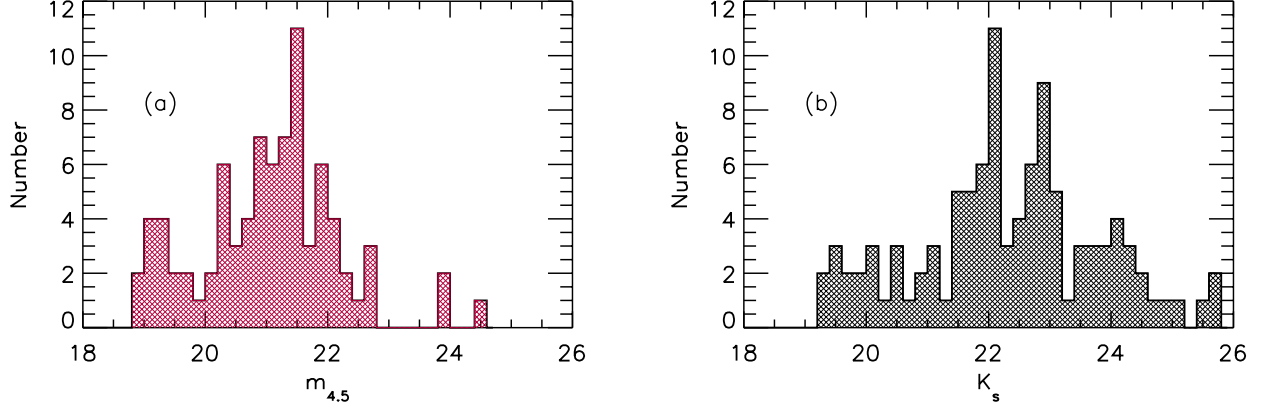


Figure 11. Distribution of (a) $4.5\,\mu\text{m}$ and (b) K_s ($2.1\,\mu\text{m}$) magnitudes. All SCUBA-2 sources with accurate positions and $850\,\mu\text{m}$ fluxes above $2\,\text{mJy}$ are shown in (b), while only the sources in the deep IRAC area are shown in (a). Three sources lying on the edge of brighter $4.5\,\mu\text{m}$ sources are excluded in (a). Sources with K_s magnitudes fainter than 25.5 are shown at that magnitude in (b).

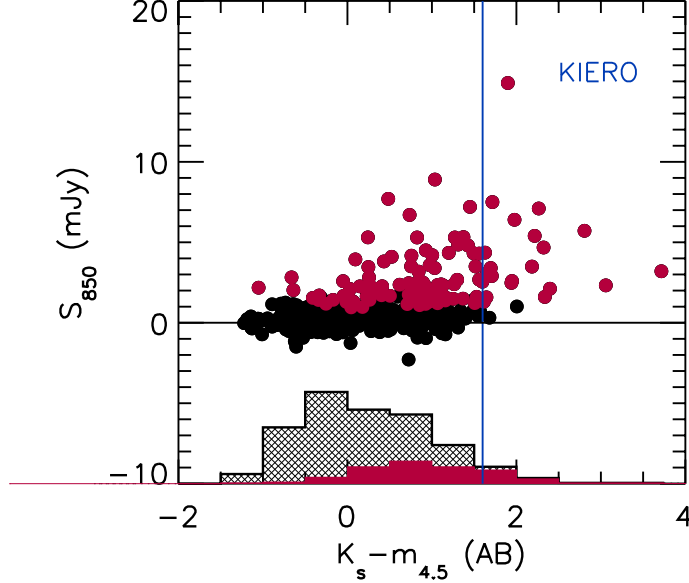


Figure 12. $850\,\mu\text{m}$ flux vs. $K_s - 4.5\,\mu\text{m}$ color for the radio sources that lie in areas of the SCUBA-2 map where the $850\,\mu\text{m}$ rms noise is $< 0.75\,\text{mJy}$. Red circles show sources detected above a 3σ threshold at $850\,\mu\text{m}$. Above the KIEROs threshold ($K_s - 4.5\,\mu\text{m} > 1.6$), 20 of the 22 radio sources are detected in the submillimeter at $> 3\sigma$. The histograms at the bottom of the plot show the $K_s - 4.5\,\mu\text{m}$ color distributions for the radio sources that are either submillimeter detected ($> 3\sigma$; red) or undetected (black shading).

optical-infrared bands (OIRTC; Chen et al. 2016).

Using the radio sample, we investigated how well the KIEROs selection works at picking out galaxies that can be detected at submillimeter wavelengths. In Figure 12, we show $850\,\mu\text{m}$ flux versus $K_s - 4.5\,\mu\text{m} > 1.6$ color for the radio sources that lie in areas of the SCUBA-2 map where the $850\,\mu\text{m}$ rms noise is $< 0.75\,\text{mJy}$. Impressively, 20 of the 22 sources that lie in the KIEROs region have submillimeter detections at the $> 3\sigma$ level (red circles). We show the color distributions for the submillimeter detected ($> 3\sigma$; red) and undetected (black shading) radio sources at the bottom of the plot.

We do not consider the optical/NIR colors further in this paper. We postpone a more detailed discussion of the SEDs in this wavelength range to a later paper in the series, where we will use the combined GOODS-N and GOODS-S datasets.

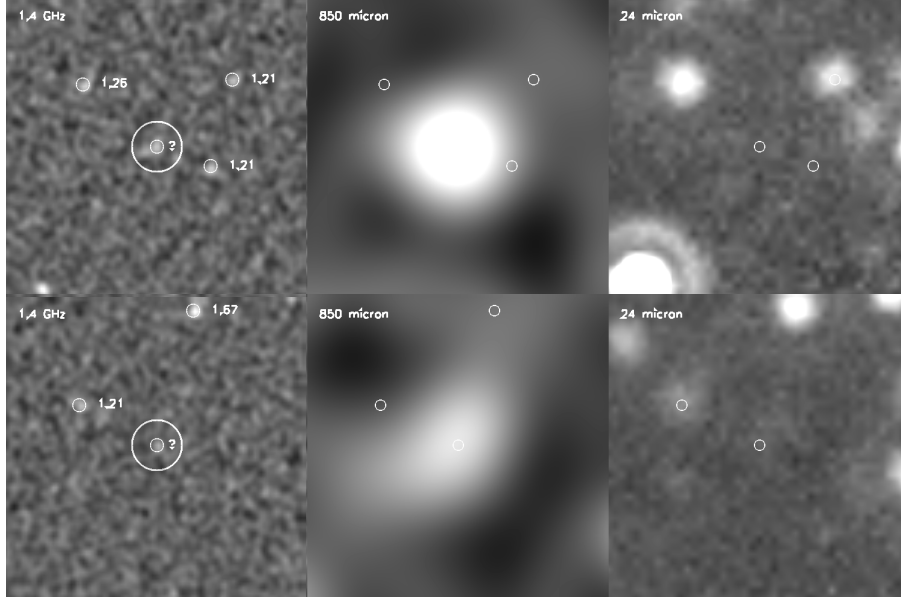


Figure 13. Brightest 2 of the 3 SCUBA-2 sources without detected $24\mu\text{m}$ counterparts (i.e., identification numbers 7 and 29 in Table 5). (Left) Radio image with the detected radio sources marked with small circles and their known spectroscopic redshifts labeled. (Center) SCUBA-2 image. (Right) $24\mu\text{m}$ image with the detected radio sources marked with small circles. Thumbnails are $50''$ on a side, and the larger circle is $4''$ in radius, which is roughly the SCUBA-2 positional uncertainty.

2.6. MIR and FIR Fluxes

We used the catalogs of Magnelli et al. (2011) to obtain the *Spitzer* MIPS $24\mu\text{m}$ and $70\mu\text{m}$ fluxes. These catalogs were constructed using $24\mu\text{m}$ data from the *Spitzer* GOODS Legacy program (PI: M. Dickinson) and $70\mu\text{m}$ data from a combination of two *Spitzer* GO programs (PI: D. Frayer), the *Spitzer* Far-Infrared Deep Extragalactic Legacy (FIDEL) program (PI: M. Dickinson), and *Spitzer* guaranteed time observer (GTO) programs (PI: G. Rieke). We used the catalogs of Magnelli et al. (2013) to obtain the *Herschel* PACS $100\mu\text{m}$ and $160\mu\text{m}$ fluxes. These catalogs were constructed using the combined data sets of the PACS Evolutionary Probe (PEP; Lutz et al. 2011) guaranteed time key program and the GOODS-*Herschel* (Elbaz et al. 2011) open time key program. We also used the wider area *Herschel* SPIRE $250\mu\text{m}$, $350\mu\text{m}$, and $500\mu\text{m}$ catalogs from Elbaz et al. (2011). Elbaz et al. (2011) and Magnelli et al. (2013) both used $24\mu\text{m}$ priors to deblend the *Herschel* data when constructing their catalogs. They provide a detailed discussion of the robustness of the $24\mu\text{m}$ priors in deblending the longer wavelength data. They also provide flags to assess whether sources are contaminated by nearby brighter sources. All but three of the SCUBA-2 sources in the GOODS-*Herschel* region have $24\mu\text{m}$ counterparts, allowing us to obtain directly the fluxes from the Elbaz et al. and Magnelli et al. catalogs for our SCUBA-2 sample. In Figure 13, we show the two brightest examples out of the three SCUBA-2 sources that do not have $24\mu\text{m}$ counterparts. Since these sources are isolated, following Barger et al. (2015), we used matched-filter extractions to measure the FIR fluxes for these sources.

2.7. Redshifts

In our efforts to obtain redshifts for the SCUBA-2 sources with accurate positions, we draw on a new compilation of known spectroscopic redshifts in the region (A. Barger et al. 2017, in preparation; see also Cohen et al. 2000; Cowie et al. 2004; Wirth et al. 2004, 2015; Swinbank et al. 2004; Chapman et al. 2005; Treu et al. 2005; Reddy et al. 2006; Barger et al. 2008; Pope et al. 2008; Trouille et al. 2008; Cooper et al. 2011). This compilation includes our own reductions of the *HST* grism data of the GOODS-N (PI: B. Weiner; Momcheva et al. 2016) (see Cowie et al. 2016 for details), but only four SCUBA-2 sources with accurate positions have grism redshifts, and all four already had ground-based optical spectroscopic redshifts. We also use CO spectroscopic redshifts from Daddi et al. (2009a,b), Walter et al. (2012), and Bothwell et al. (2013).

Additionally, we made observations with MOSFIRE on Keck I of 39 of the SCUBA-2 sources. We focused these observations on those sources without redshift identifications but with accurate positions. We used a $0''.7$ slit width and

observed in the J (24 min exposure), H (16 min), and K (24 min) bands using an ABBA stepping pattern, where the A position is $1''.25$ below the nominal position, and the B position is $1''.25$ above the nominal position. A description of the reduction procedures that we used can be found in Cowie et al. (2016). We spectroscopically identified 9 SCUBA-2 sources based on the [NII]6584 and $H\alpha$ lines and the [OIII]5007/ $H\beta$ complex.

Where there is no spectroscopic redshift, we use photometric redshifts from Rafferty et al. (2011). Half of the SCUBA-2 galaxies with accurate positions (57 of 114) have spectroscopic or photometric redshifts. A significant number of the spectroscopic redshifts come from the work of Swinbank et al. (2004) and Chapman et al. (2005), who used radio priors to identify SCUBA galaxies in the CDF-N. However, it is worth noting that a substantial fraction of the sources in these samples turn out not to be detected in our SCUBA-2 map. In Table 4, we take from the Chapman et al. paper the right ascension and declination (Columns 1 and 2), the radio flux (from Richards 2000) (Column 3), the SCUBA flux, error, and S/N (Columns 4–6), and the redshift (Column 7) for the galaxies that lie in our SCUBA-2 field, followed by the current radio flux (Column 8), the SCUBA-2 flux, error, and S/N (Column 9–11), and the current redshift (Column 12). A small number of the previous redshifts were incorrect and were updated in subsequent work.

One of the Chapman et al. (2005) sources is not present in the current radio observations, and a further eight (out of the total of twenty) are not confirmed as SCUBA-2 sources. These eight are high radio power sources without genuine submillimeter detections, either because the submillimeter emission came from another radio source, or else because it was simply a noise spike in the SCUBA data. This effect only slightly increases the median redshift of the submillimeter detected sources in this sample (from $z = 2.0$ to $z = 2.1$).

Table 4. Chapman et al. (2005) Sample

R.A. (J2000.0)	Decl. (J2000.0)	20 cm Flux (μ Jy)	SCUBA Flux (mJy)	SCUBA Error (mJy)	SCUBA S/N	z	Current 20 cm Flux (μ Jy)	SCUBA-2 Flux (mJy)	SCUBA-2 Error (mJy)	SCUBA-2 S/N	Current z
(1)	(2)	(3)	(4)	(5)	(6)	(7)	(8)	(9)	(10)	(11)	(12)
189.07637	62.264027	151.	7.30	1.10	6.63	1.865	169	7.1	0.69	10.	2.000
189.09438	62.274918	70.9	7.70	1.30	5.92	2.466	81.	4.0	0.41	9.7	1.790
189.21568	62.205917	49.3	4.60	0.800	5.75	0.2980	62.	0.33	0.29	1.1	0.3000
189.06729	62.253807	53.9	5.80	1.10	5.27	2.578	38.	3.4	0.60	5.6	2.578
189.30020	62.203415	21.0	8.00	1.80	4.44	2.914	32.	5.3	0.89	5.8	2.914
189.13586	62.133358	90.6	5.50	1.30	4.23	1.993	63.	0.15	0.48	0.32	1.994
188.97192	62.227139	58.4	8.80	2.10	4.19	2.098	40.	4.3	0.80	5.3	2.098
189.08862	62.285667	148.	7.80	1.90	4.10	1.988	164	3.4	0.60	5.6	1.988
189.14830	62.240025	87.8	5.50	1.40	3.92	2.005	78.	4.8	0.35	13.	2.005
189.12137	62.179386	81.4	5.00	1.30	3.84	1.013	91.	0.27	0.40	0.68	1.013
189.15312	62.198914	39.0	7.00	2.10	3.33	0.5570
188.95601	62.260220	74.6	8.30	2.50	3.32	2.203	87.	3.3	0.80	4.1	2.203
189.02855	62.172611	74.4	11.6	3.50	3.31	2.505	72.	-0.37	0.54	-0.68	2.505
189.00063	62.179779	131.	7.90	2.40	3.29	1.994	123	-0.18	0.70	-0.26	2.002
189.02798	62.264084	24.0	4.40	1.40	3.14	2.416	13.	1.7	0.50	3.4	2.413
189.28004	62.235580	45.0	4.70	1.50	3.13	2.484	58.	7.0	1.4	5.0	2.490
189.34113	62.176472	41.0	12.0	3.90	3.07	0.9790	58.	0.56	0.41	1.3	0.9781
189.14380	62.211388	230.	4.30	1.40	3.07	1.219	188	2.8	0.34	8.2	1.224
189.29991	62.223808	53.9	4.20	1.40	3.00	1.996	55.	-0.60	0.34	-1.7	1.996
188.97975	62.150475	212.	5.40	1.90	2.84	1.875	179	-0.24	0.81	-0.30	1.875

2.8. Catalog

In Table 5, we give the SCUBA-2 $850\mu\text{m}$ catalog. While submillimeter and millimeter samples are often extended to lower significance, we restrict to sources detected at or above a 4σ threshold, relative to the statistical noise, in order to provide a robust, well-determined sample that minimizes the inclusion of spurious sources. The catalog is ordered by $850\mu\text{m}$ flux.

We give an identification number (Column 1), a name based on the SCUBA-2 coordinate (Column 2), the right

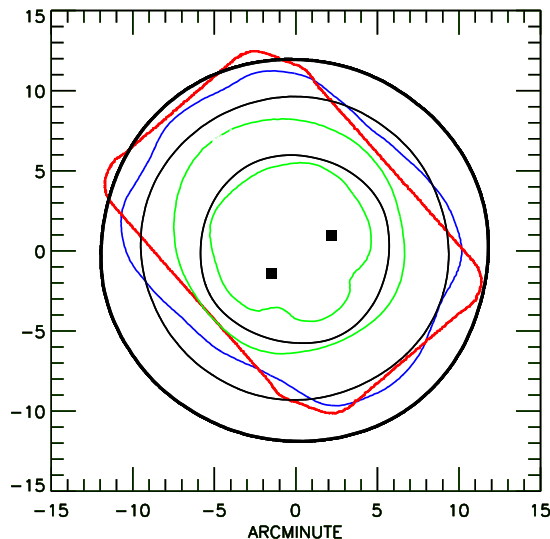


Figure 14. Comparison of the areas covered by recent wide-field surveys. The black contours show the present SCUBA-2 image (center contour— $850\,\mu\text{m}$ rms noise level of $0.5\,\text{mJy}$; middle contour— $1\,\text{mJy}$; outer contour— $1.5\,\text{mJy}$). The central rms noise is $0.28\,\text{mJy}$. The green contours show the S2CLS image (center contour— $850\,\mu\text{m}$ rms noise level of $1\,\text{mJy}$; outer contour— $1.25\,\text{mJy}$). The central rms noise is $0.83\,\text{mJy}$. The outer counter corresponds roughly to the outside edge of the S2CLS image. The blue contour shows the combined AzTEC+MAMBO image at a $1.16\,\text{mm}$ rms noise level of $1\,\text{mJy}$. The central rms noise is $0.53\,\text{mJy}$. We also show the area observed with the *Herschel* PACS survey (red contour), as well as the two sources detected above the 4σ threshold in the GISMO $2\,\text{mm}$ survey of the central region.

ascension and declination measured from the SCUBA-2 image (Columns 3 and 4), and the $850\,\mu\text{m}$ flux, error, and S/N (Columns 5–7). For each source, we have found all the SMA and radio sources within a $4''.5$ radius of the SCUBA-2 source. If there is an SMA detection or a single radio source in the area, then we give this accurate right ascension and declination (Columns 8 and 9). SMA identifications are the most robust and can be identified by the SMA flux given in Column 10. We give the $20\,\text{cm}$ flux in Column 11 for all the sources with accurate coordinates. For SCUBA-2 sources with no radio source in the area, we give 5σ upper limits on the $20\,\text{cm}$ flux ($< 12\,\mu\text{Jy}$). The remaining sources without radio fluxes have multiple radio sources in the area, so a unique identification is only possible with SMA follow-up. Thus, we do not give a radio flux for these. For sources with accurate positions, we give the K_s magnitude measured from the image of Wang et al. (2010) (Column 12), a spectroscopic (or photometric) redshift, if available, with the corresponding literature source (Column 13), and a $250\,\mu\text{m}/850\,\mu\text{m}$ redshift estimate (Column 14; see Section 3.2 for details). We use only 2 decimal places for the photometric redshifts given in Column 13 in order to distinguish them from the spectroscopic redshifts.

In Table 6, we give the SCUBA-2 $450\,\mu\text{m}$ catalog. We list only the sources detected at or above a 4σ threshold in the region where the $450\,\mu\text{m}$ noise is less than $10\,\text{mJy}$ (see Figure 2). The format is the same as in Table 5, except that in the final column, we give the $850\,\mu\text{m}$ flux measured at the $450\,\mu\text{m}$ position, rather than the $250\,\mu\text{m}/850\,\mu\text{m}$ redshift estimate.

2.9. Comparison with Previous Wide-field Observations

Out of the $186 \geq 4\sigma$ $850\,\mu\text{m}$ sources given in Table 5, 38 had previously been found (with $850\,\mu\text{m}$ SCUBA observations, Wang et al. 2004 and Pope et al. 2005; $1.1/1.2\,\text{mm}$ AzTEC and MAMBO observations, Penner et al. 2011; and $2\,\text{mm}$ GISMO observations, Staguhn et al. 2014). We summarize these previous results in Table 7. In general, the agreement in the fluxes is good for the high flux sources, but some of the fainter flux sources have significant upward biases in the SCUBA fluxes.

More recently, the SCUBA2 Cosmology Legacy Survey (S2CLS) has presented a SCUBA-2 based catalog of the region (Geach et al. 2017). This survey is considerably shallower than the present data and also covers a smaller area. In Figure 14, we show the S2CLS area (green) compared with our survey (black). For comparison, we also show the $1.16\,\text{mm}$ area of Penner et al. (2011; blue) and the *Herschel* PACS area of Elbaz et al. (2011; red). As summarized in Table 7, nearly all of the brighter sources in the overlap areas are in good agreement.

As we discussed in Section 2.7 (see Table 4), there are a number of SCUBA sources—some even with moderately high significance—that are not detected in the present SCUBA-2 data. For example, of the five sources in the HDF-N SCUBA image of Hughes et al. (1998; they use HDF850 names), only two (HDF850.1 and HDF850.2) appear to be

real, with the remaining sources being noise spikes in the SCUBA data. This carries through to subsequent, more extensive catalogs in the larger CDF-N region.

In Figure 15, we compare the fluxes of some literature samples with our SCUBA-2 sample. We show the $\geq 4.5\sigma$ SCUBA samples of (a) Pope et al. (2005; they use GN names) and (b) Wang et al. (2004; they use GOODS850 names), as well as the $\geq 4.5\sigma$ S2CLS sample of 29 sources from (c) Geach et al. (2017). When a literature source is also in our SCUBA-2 catalog, then we plot the literature flux versus our SCUBA-2 flux. When a literature source is not also in our SCUBA-2 catalog, then we use a nominal SCUBA-2 flux of 0.5 mJy. We mark sources with radio counterparts within the beam with red circles and other sources with black squares.

In each of the SCUBA samples, there are SCUBA-2 undetected sources: GN1, GN8, and GN13 (GN13 is also known as GOODS850-10 and HDF850.4), GOODS850-4, GOODS850-8, GOODS850-13, and GOODS850-14. (Note that the two samples were constructed from heavily overlapped data sets.) Since none of these sources is seen in the combined AzTEC+MAMBO 1.16 mm image of Penner et al. (2011), they are likely all spurious.

The average SCUBA flux of the sources detected by both SCUBA and SCUBA-2 relative to the average SCUBA-2 flux for these same sources is 20% higher for the Pope et al. (2005) measurements and 10% higher for the Wang et al. (2004) measurements. The slightly higher fluxes measured by SCUBA are likely a consequence of the Eddington bias in the SCUBA selection, since we use raw rather than corrected (de-boosted) fluxes in the comparison.

All 29 S2CLS sources with $S/N \geq 4.5$ are in our SCUBA-2 catalog. (Below this threshold, we detect only about 70% of the S2CLS sources.) Our 850 μm fluxes are about 2.5% lower, on average, than those in S2CLS, which is well within the calibration uncertainty of the SCUBA-2 data.

Recently, Shu et al. (2016) used a comparison of the 24 μm *Spitzer* observations with the 500 μm *Herschel* observations to construct a sample of high-redshift 500 μm selected galaxies. 33 of the 36 sources that they selected are in our 850 μm sample, while two of the remaining three sources lie close to bright SCUBA-2 sources and hence are contaminated. The final source is not strongly detected in the SCUBA-2 image. Their high-redshift candidate sample can therefore be considered a subsample of the present data.

2.10. Measuring Submillimeter Fluxes for Other Samples

In determining the SCUBA-2 fluxes for other samples, such as X-ray and optical, we used priors from the SMA and radio data to minimize contamination by neighboring bright sources in the field. The procedure is as follows. For target sample sources within $2''$ of an SMA detected source (see Table 3), we used the SMA flux. We constructed a de-blended SCUBA-2 image with sources at the SMA positions removed using the measured SCUBA-2 PSFs and fluxes. We measured the SCUBA-2 fluxes for the radio sample in this cleaned image, and, as a function of flux down to a detection level of 3σ , iteratively removed these fluxes from the SCUBA-2 image. For sources in the target sample within $2''$ of a SCUBA-2 detected radio source, we assigned the SCUBA-2 flux of the radio source. Finally, we measured the fluxes of the remaining sources directly at their positions in the SCUBA-2 image cleaned of both SMA and radio sources. The procedure can also be run on blank field (random) samples to measure the biasing and contamination levels. For the 450 μm data, where the image is shallower and where we are far from the confusion limit, we simply measured the 450 μm flux in the matched filter SCUBA-2 image at the nominal position of the target sample source. Although other samples are not used in the current paper, they will be used in subsequent papers in this series.

3. DISCUSSION

3.1. Spectral Energy Distributions: Converting to Star Formation Rates

For the higher redshift galaxies (i.e., $z > 1.2$), we expect that the observed-frame 850 μm flux will approximate the FIR luminosity independent of redshift, since the strong negative K -correction almost exactly offsets the effects of distance (e.g., Blain et al. 2002; Casey et al. 2014). The exact conversion depends on the SED of the source.

Barger et al. (2014) showed that the SEDs of nearly all high-redshift SCUBA-2 galaxies are very similar to those of Arp 220 at least at the longer wavelengths. We illustrate this again in Figure 16, where we show the quantity $L_\nu \nu$ normalized to the observed-frame 850 μm flux for the 12 brightest SCUBA-2 galaxies with spectroscopic redshifts $z > 1.2$, 850 μm fluxes > 3 mJy, and $S/N > 5$ and that lie in the more sensitive regions of the GOODS-*Herschel* observations. Nearly all of these are isolated sources, as we illustrate in Figure 17 where we show the thumbnail images at 850, 450, 250, 100, and 24 μm . The deblending using the 24 μm priors is only important in a small number of sources (identification numbers 8 and 26). Each galaxy in Figure 16 is color coded. For cases where there is no detection in a band, we show a 2σ upper limit and a downward pointing arrow. For comparison, we show the Arp 220 SED given by Silva et al. (1998) (red curve). We also show a graybody fit to Arp 220 (a single temperature of 43 K and an emissivity index of $\beta = 1.25$; blue curve), which is a very good approximation to the observed SEDs (all of the

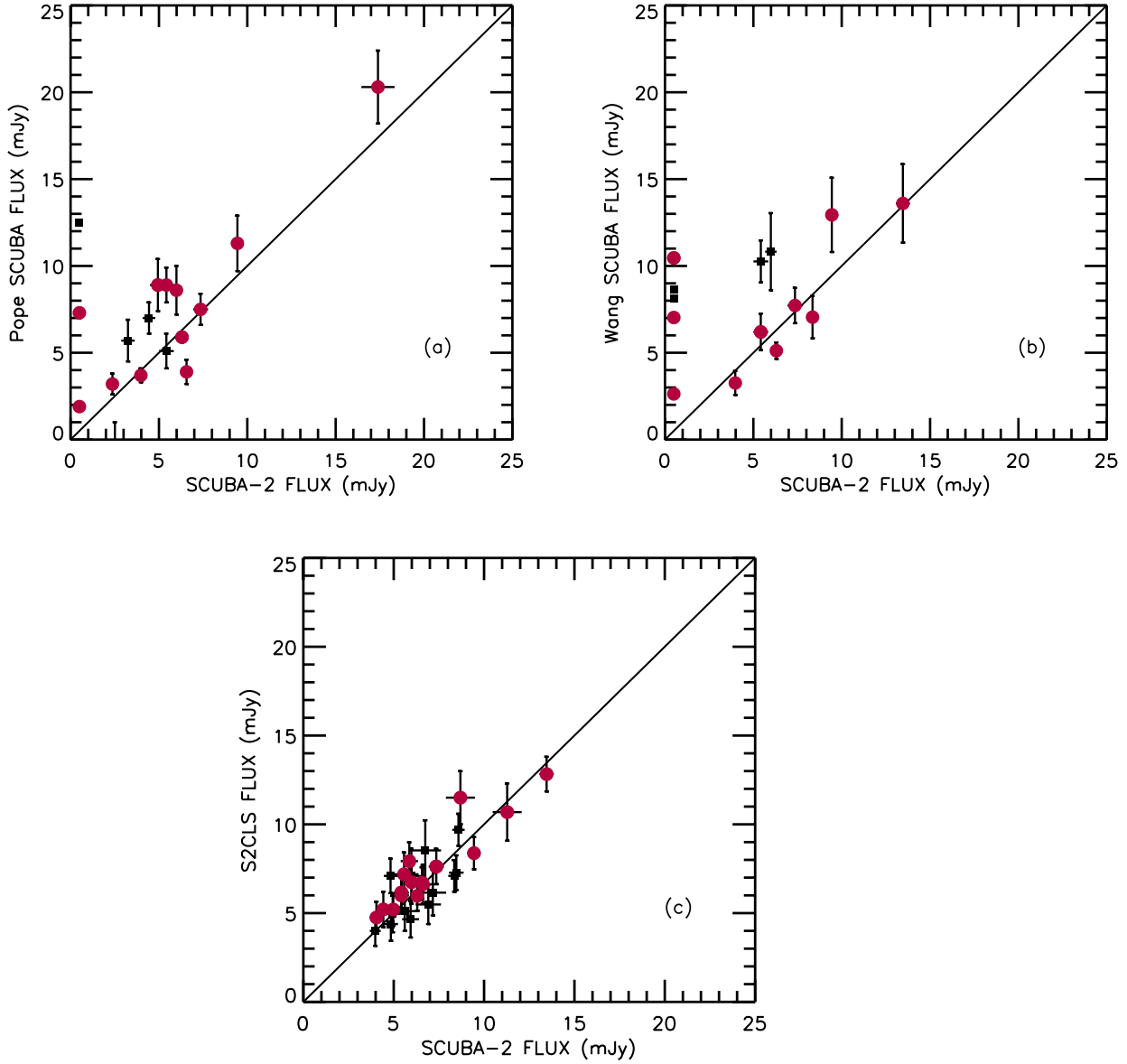


Figure 15. SCUBA 850 μm flux from the $S/N \geq 4.5$ SCUBA samples of (a) Pope et al. (2005) and (b) Wang et al. (2004) vs. our SCUBA-2 850 μm flux. There are three undetected sources in (a) and five in (b). (c) S2CLS 850 μm flux from Geach et al. (2017) for the 29 sources in their sample with $S/N \geq 4.5$ vs. our SCUBA-2 850 μm flux. All of these sources are detected. In each case, we mark sources with radio counterparts in the beam with red circles and other sources with black squares. Literature sources not detected in our SCUBA-2 data are shown at a nominal value of 0.5 mJy in the x -axis. The error bars are 1σ . The SCUBA-2 (x -axis) errors are smaller than the symbol sizes for many of the sources.

points lie within a multiplicative factor of 1.8) down to $\sim 50\mu\text{m}$. This is similar to da Cunha et al. (2015)’s result that the typical ALESS (i.e., ALMA follow-up survey of the single-dish LABOCA 870 μm survey of the Extended Chandra Deep Field South) source has a luminosity-averaged dust temperature of $43 \pm 2\text{ K}$. In order to fit the shorter wavelengths that are dominated by hot dust emission, the fit would need to be extended with a MIR power law (e.g., Casey 2012).

To determine the conversion from observed-frame 850 μm flux ($S_{850\mu\text{m}}$) to $L_{8-1000\mu\text{m}}$ luminosity, we interpolated between the individual $\log L_{\nu}\nu$ points and then integrated to obtain $L_{8-1000\mu\text{m}}$. The number of data points is sufficiently large to make this procedure robust, and it avoids fitting model or template SEDs. In Figure 18, we show $L_{8-1000\mu\text{m}}$ versus $S_{850\mu\text{m}}$ for the 26 SCUBA-2 galaxies with accurate positions and spectroscopic redshifts (circles).

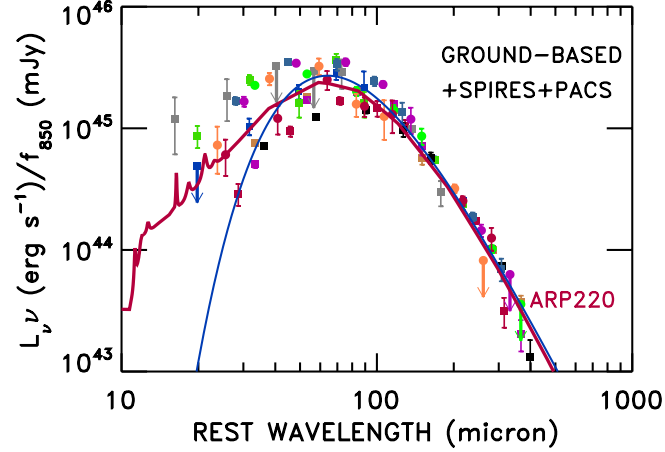


Figure 16. SEDs for the 12 SCUBA-2 galaxies with spectroscopic redshifts $z > 1.2$, $850\,\mu\text{m}$ fluxes $> 3\,\text{mJy}$, and $S/N > 5$. (Identification number 10 in Table 5, also known as GN20.2, is excluded, since it lies close to identification number 2, also known as GN20.) All of the SEDs are normalized to the observed-frame $850\,\mu\text{m}$ flux. Each galaxy is individually color coded and shows seven L_ν points at the rest-frame wavelengths corresponding to the 100, 160, 250, 350, 450, 850, and $1100\,\mu\text{m}$ bands. Non-detections in a band are shown with a 2σ upper limit and a downward pointing arrow. The red curve shows the corresponding shape of Arp 220 from Silva et al. (1998), while the blue curve shows a graybody fit to Arp 220 with a temperature of 43 K and $\beta = 1.25$.

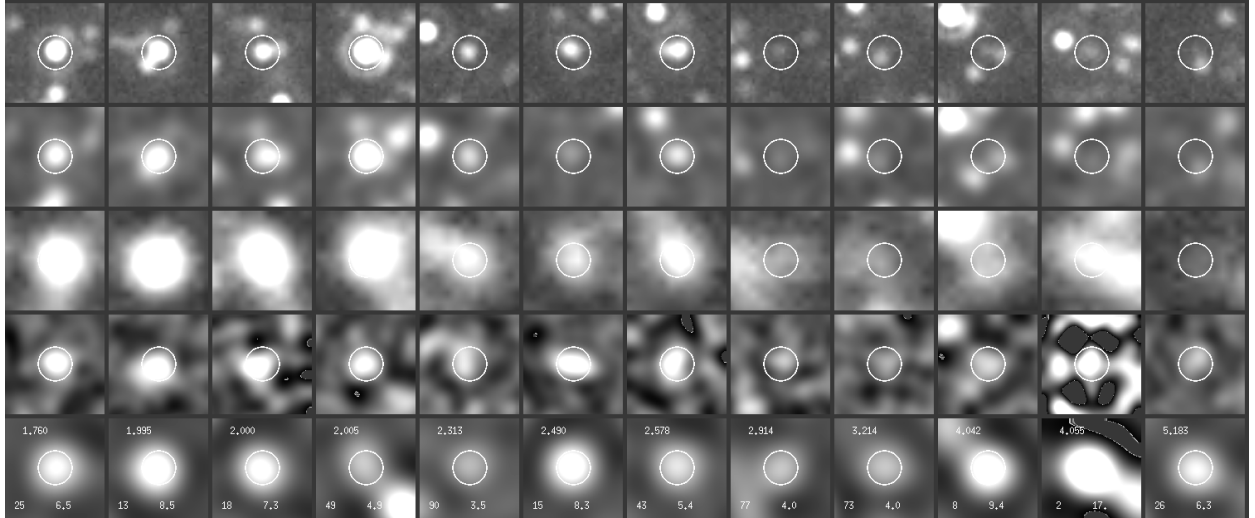


Figure 17. Thumbnails for the 12 SCUBA-2 galaxies with spectroscopic redshifts $z > 1.2$, $850\,\mu\text{m}$ fluxes $> 3\,\text{mJy}$, and $S/N > 5$ that are shown in Figure 16. The panels from bottom to top show the observations at 850, 450, 250, 100, and $24\,\mu\text{m}$. The identification number (from Table 5), SCUBA-2 $850\,\mu\text{m}$ flux, and redshift are given for each source in the bottom panel. The panels are shown in ascending order of redshift from left to right. The fluxes at shorter wavelengths drop rapidly with increasing redshift.

We determine a mean conversion of

$$\log L_{8-1000\,\mu\text{m}} (\text{erg s}^{-1}) = \log S_{850\,\mu\text{m}} (\text{mJy}) + 45.60 \pm 0.05, \quad (3)$$

where we have computed the 1σ error using the jackknife resampling statistic. The median would give a conversion of 45.57 (blue line in Figure 18). All of the sources lie within a multiplicative factor of 2 of this relation (shaded region).

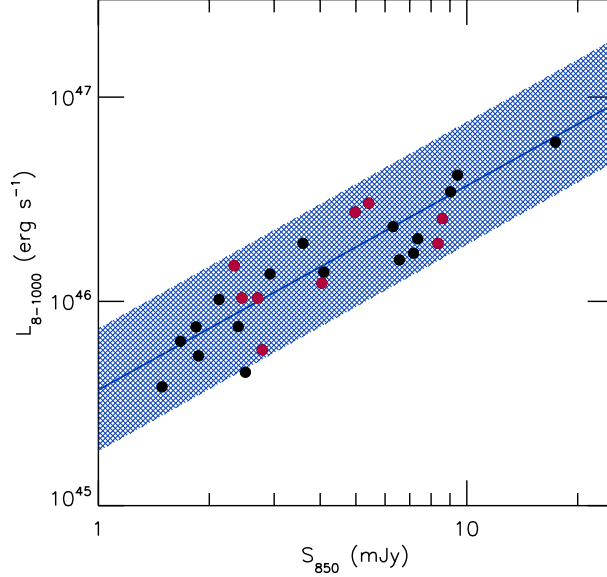


Figure 18. FIR ($8-1000\ \mu\text{m}$) luminosity vs. $850\ \mu\text{m}$ flux (circles) for the 26 SCUBA-2 galaxies in the more sensitive regions of the GOODS-*Herschel* coverage (less than 2 times the minimum noise) with accurate positions and spectroscopic redshifts. The blue line shows a linear relation based on the median ratio, while the shaded region shows a spread by a multiplicative factor of two about this line. Red circles show galaxies that would be classified as containing an AGN based on having rest-frame $2-8\ \text{keV}$ luminosities $> 10^{43}\ \text{erg s}^{-1}$.

For the SCUBA-2 galaxies, $L_{8-1000\ \mu\text{m}}$ approximates the bolometric luminosity. Thus, to get a SFR from $S_{850\ \mu\text{m}}$, we adopt the theoretical conversion of Murphy et al. (2011) between $L_{8-1000\ \mu\text{m}}$ and SFR (their Equation 4), namely,

$$\log \text{SFR}(M_{\odot}\ \text{yr}^{-1}) = \log L_{8-1000\ \mu\text{m}}(\text{erg s}^{-1}) - 43.41. \quad (4)$$

They computed this conversion from Starburst99 (Leitherer et al. 1999) for a constant SFR and a Kroupa (2001) IMF. Madau & Dickinson (2014) adopted a slightly lower conversion of -43.55 (after converting from their adopted Salpeter 1955 IMF to a Kroupa IMF), which should be taken into account when comparing with their SFRs (see Section 3.4). Now, combining Equations 3 and 4, we get

$$\text{SFR}(M_{\odot}\ \text{yr}^{-1}) = 143 \pm 20 \times S_{850\ \mu\text{m}}(\text{mJy}). \quad (5)$$

This conversion should be adequate for a Chabrier (2003) IMF, as well, but for a simple power law Salpeter (1955) IMF with power law index -2.35 and mass limits 0.1 and 100 solar masses, the normalization would rise to 230 ± 32 . This Salpeter conversion is consistent with that given in Barger et al. (2014).

Some portion of the shorter wavelength SCUBA-2 SEDs could be contributed by AGN activity. As can be seen from Figure 18, there is no clear difference in the bolometric luminosities of the SCUBA-2 galaxies with known X-ray detections (red circles have rest-frame $2-8\ \text{keV}$ luminosities $> 10^{43}\ \text{erg s}^{-1}$)—suggesting they contain AGNs—versus those without, so this effect is not large for AGNs that are not very Compton thick. Emission from an AGN torus is also not likely to contribute significantly above $\sim 100\ \mu\text{m}$ (Fritz et al. 2006; Netzer et al. 2007; Schartmann et al. 2008; Hönig & Kishimoto 2010; Mullaney et al. 2011; Siebenmorgen et al. 2015), so the longer wavelength contributions to the bolometric luminosity should not be affected by AGN activity. Thus, the maximum correction for any AGN contributions would likely be smaller than the multiplicative factor of two already ascribed. We will return to the issue of the AGN contributions in Paper 3 of the series using the much deeper X-ray observations in the CDF-S.

3.2. Redshift Estimators

Historically, the most popular method for estimating redshifts for submillimeter detected galaxies without spectroscopic or photometric redshifts was to use the ratio of the $20\ \text{cm}$ flux to the $850\ \mu\text{m}$ flux (Carilli & Yun 1999; Barger et al. 2000, who called these millimetric redshifts). It was thought that using a FIR flux to submillimeter flux ratio to estimate redshifts would not work, given the expectation at the time of a wide range of temperatures in submillimeter

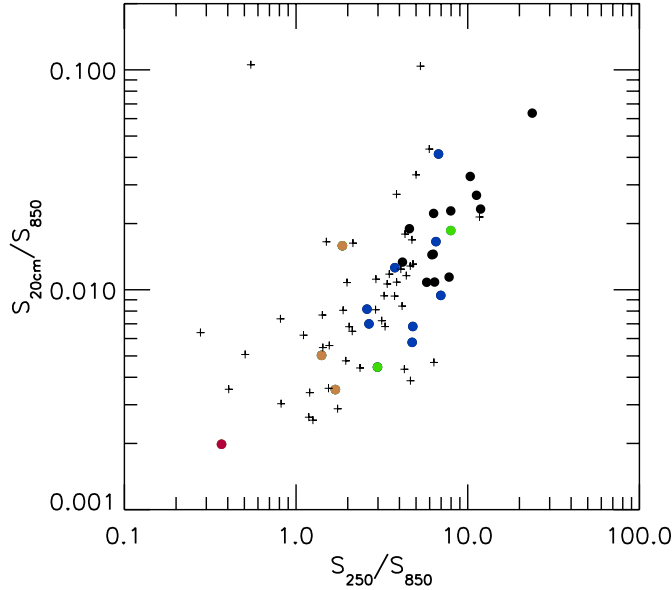


Figure 19. 20 cm/850 μm flux vs. 250 μm /850 μm flux. There is a good relation between the two flux ratios, and the sources with spectroscopic redshifts are well segregated by redshift (circles: black— $z < 2$, blue— $z = 2 - 3$, green— $z = 3 - 4$, gold— $z = 4 - 5$, red— $z = 5 - 6$). SCUBA-2 sources without spectroscopic redshifts but with accurate positions are denoted by crosses. The two sources at the top of the plot that lie off the correlation are high radio power sources where the radio power is not related to star formation.

detected galaxies. However, since we have found that these bright SCUBA-2 selected galaxies have relatively uniform SEDs at the longer rest-frame wavelengths (see Section 3.1), this opens up the possibility of using the shape of the SED to estimate redshifts (e.g., Chakrabarti et al. 2013).

We only have full SED information in the GOODS-*Herschel* region. However, the 250 μm , 350 μm , and 500 μm data from Elbaz et al. (2011) cover the full SCUBA-2 field. Since the sources outside the GOODS-*Herschel* region are not contained in the Elbaz et al. catalogs, following Barger et al. (2015), we used matched-filter extractions to measure the FIR fluxes for these sources. Here we investigate how well a two-color redshift estimator works for determining redshifts for the SCUBA-2 sample; specifically, we use the ratio of the 250 μm flux to the 850 μm flux.

In Figure 19, we compare the 20 cm/850 μm flux ratio with the 250 μm /850 μm flux ratio. Both ratios are well correlated, which suggests that both provide a measure of the redshifts. Sources without spectroscopic redshifts but with accurate positions are denoted by crosses, while sources with spectroscopic redshifts are color-coded by redshift interval (circles; see figure caption for intervals). The sources with spectroscopic redshifts are indeed well segregated by redshift interval in the plot. There are two high radio power sources at the top of the plot that lie off the correlation, which illustrates how there can be submillimeter detected sources where the radio power is not produced by star formation (see Barger et al. 2017).

To see more clearly how well each flux ratio does at estimating reliable redshifts, in Figure 20, we plot spectroscopic redshift versus (a) 250 μm /850 μm flux ratio and (b) 20 cm/850 μm flux ratio. In (a), the red curve shows the 250 μm /850 μm flux ratio versus redshift for an Arp 220 SED, while the blue curve shows the relation

$$z_{250} = 4.20 - 3.14 \log(S_{250 \mu\text{m}}/S_{850 \mu\text{m}}) + 0.352 \log(S_{250 \mu\text{m}}/S_{850 \mu\text{m}})^2, \quad (6)$$

which is based on a quadratic fit to the logarithmic flux ratio. In (b), the blue curve shows the redshift relation from Barger et al. (2000; the ratio of their Equations 2 to 4) for an Arp 220 SED. The scatter in Figure 20(b) is considerably larger than the scatter in Figure 20(a). It is clear that the radio power is not always an accurate measure of the star formation. The scatter in Figure 20(a) is primarily caused by the variations in the SEDs of the sources (see Figure 16).

In Figure 21, we show (a) photometric, (b) z_{250} (using Equation 6, so there is no SED assumption), and (c) millimetric redshift estimates for the SCUBA-2 galaxies with $z > 1.2$ and accurate positions. The photometric redshift estimates provide the best approximation to the spectroscopic redshifts, but they cannot be computed for the highest redshift

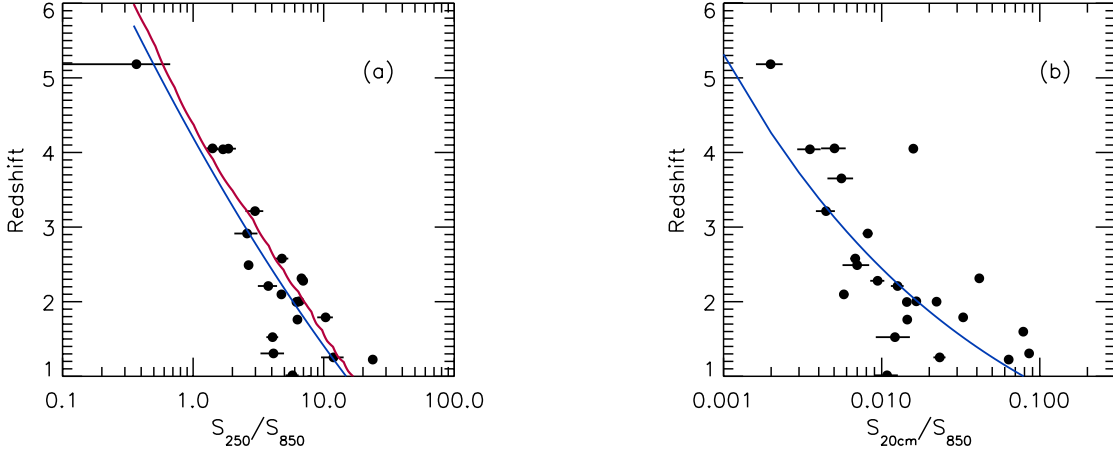


Figure 20. (a) Spectroscopic redshift vs. $250\ \mu\text{m}/850\ \mu\text{m}$ flux ratio (black circles). The red curve shows the redshift vs. the same flux ratio for an Arp 220 SED, while the blue curve shows a fit of the form given in Equation 6. (b) Spectroscopic redshift vs. $20\ \text{cm}/850\ \mu\text{m}$ flux ratio. The blue curve shows the redshift relation from Barger et al. (2000) for an Arp 220 SED.

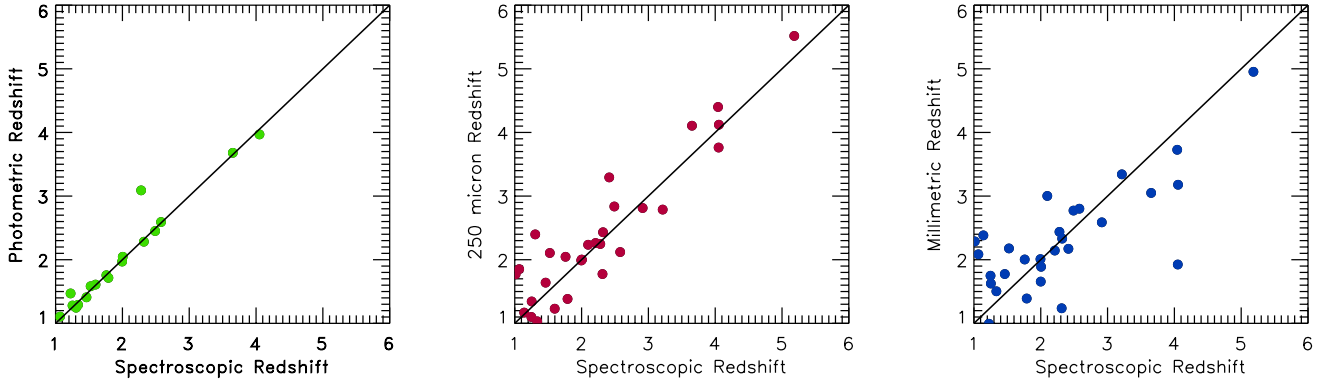


Figure 21. Comparison of (a) photometric (green circles), (b) $250\ \mu\text{m}/850\ \mu\text{m}$ (red circles), and $20\ \text{cm}/850\ \mu\text{m}$ (blue circles) redshift estimates vs. spectroscopic redshifts for the SCUBA-2 galaxies with $z > 1.2$ and accurate positions.

galaxies detected in the submillimeter, which are too faint in the optical/NIR. The z_{250} redshift estimates can be extended to all of the SCUBA-2 galaxies (though some are not detected at $250\ \mu\text{m}$, providing only lower limits on the redshifts). Note that these will be most reliable for galaxies at $z \gg 1$. Although the millimetric redshift estimates are not as good as z_{250} , they can still be used to test z_{250} .

3.3. Redshift Distributions

By adopting z_{250} , we can use all the sources from the full SCUBA-2 field in measuring the star formation history, as well as avoid any biases that might be introduced from radio matching. In Figure 22(a), we plot $850\ \mu\text{m}$ flux versus z_{250} (green circles for sources with SMA measurements; black circles otherwise). Sources without significant $250\ \mu\text{m}$ detections have only lower limits on z_{250} and are shown with right-pointing arrows in the figure based on the 1σ limit on the $250\ \mu\text{m}$ flux. We show with blue horizontal lines and right-hand axis labels the SFRs that correspond to the $850\ \mu\text{m}$ fluxes for a Kroupa (2001) IMF based on Equation 5. For sources with a spectroscopic redshift, we plot them again in Figure 22(b) as red circles at the values of the spectroscopic redshifts. We also plot red connectors from the spectroscopic redshifts to z_{250} (as in (a), green circles for sources with SMA measurements; black circles otherwise). Fortunately, the differences between z_{250} and the spectroscopic redshifts are generally too small to affect the determinations of the SFR distribution functions.

We note several features from Figure 22(a). First, there is a strong deficiency of luminous SCUBA-2 sources at $z \ll 2$. Nearly all of the luminous sources lie in the $z \sim 2 - 5$ range. Second, there is a tendency for the SCUBA-2 sources to lie in redshift sheets, such as the well-known spectroscopic features at $z = 1.99$ (Chapman et al. 2009) and $z = 4.05$ (Daddi et al. 2009b). Unfortunately, z_{250} is not accurate enough to decide whether additional sources lie in these sheets; only with spectroscopic redshifts is there enough velocity resolution for that. The presence of redshift

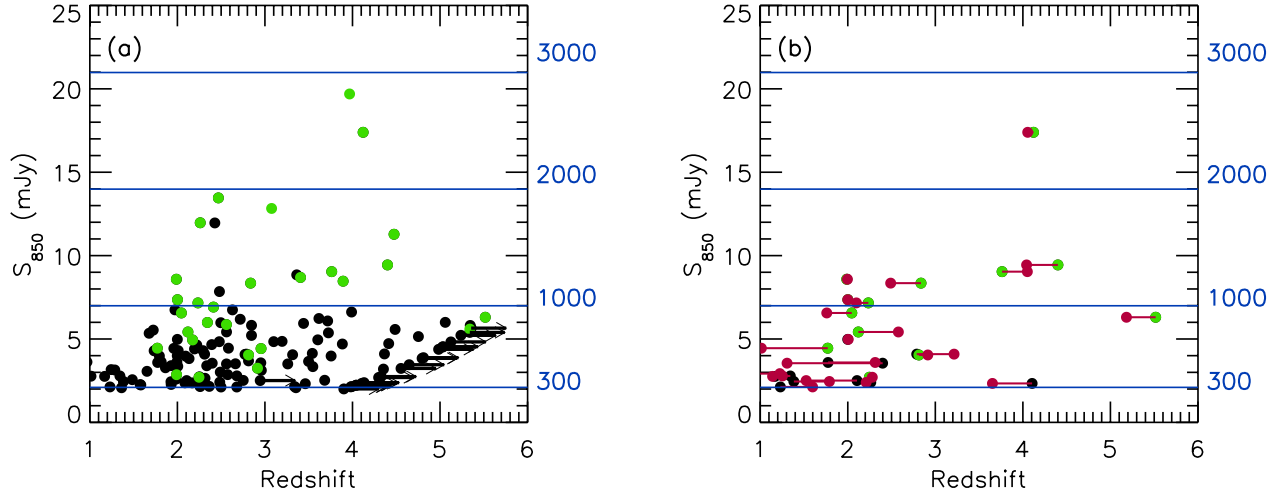


Figure 22. (a) 850 μm flux vs. z_{250} for the full sample of SCUBA-2 sources with 850 μm fluxes > 2 mJy. Where there is (is not) an SMA measurement, the source is shown with a green (black) circle. The green circles include nearly all of the brighter SCUBA-2 galaxies. Sources where there is no 250 μm detection are shown with right-pointing arrows. (b) The sample with spectroscopic redshifts. The red circles are plotted at the spectroscopic redshifts and then connected with red lines to the corresponding black or green circles plotted at z_{250} . The blue horizontal lines and right-hand axis labels in both panels show the SFRs for a Kroupa (2001) IMF.

sheets emphasizes the problem of cosmic variance in determining the star formation history, and we postpone a more detailed discussion of this issue to a subsequent paper in the series.

In Figure 23, we show the redshift distribution for the 850 μm sample divided into three flux intervals: (a) 2–4 mJy, (b) 4–8 mJy, and (c) 8–20 mJy. In Figure 23(d), we also show the redshift distribution for the full 450 μm sample > 18 mJy. As expected, because of the smaller K -correction, the 450 μm sample has a relatively low redshift distribution with a median value of $z = 2.0^{+0.4}_{-0.2}$, where the superscript and subscript give the 68% confidence interval on the median. (See Béthermin et al. 2015 for an extensive discussion of the wavelength dependence of the redshift distribution of dusty, star-forming galaxies.) The 450 μm sample is too small for an analysis of the dependence of the redshift distribution on the flux. However, the median value can be compared with the median redshift of $z = 1.95 \pm 0.19$ found by Casey et al. (2013) and the mean redshift of $z = 1.3$ found by Geach et al. (2013) for samples limited at fainter fluxes of 13 mJy and 5 mJy, respectively. These results suggest that the redshift distribution at 450 μm is increasing with increasing flux.

The situation is much clearer for the larger 850 μm sample, where the redshift distribution is clearly increasing with increasing flux, as shown in Figure 24. A Mann-Whitney test gives only a 0.15% probability that the 8–16 mJy sample (Figure 23) is drawn from the same redshift distribution as the 2–4 mJy sample. A linear least squares fit gives the relation

$$z_{\text{median}} = 2.26 + 0.11(\pm 0.03) \times S_{850} \text{ (mJy)}, \quad (7)$$

which we show as the black line in Figure 24. These results are broadly consistent with recent modeling by Béthermin et al. (2015), who find lower redshift distributions for lower fluxes and shorter wavelengths.

3.4. Evolution of the SFR Density Distribution Functions with Redshift

We computed the SFR density history and the SFR density distribution functions for the SCUBA-2 sources with SFRs $\gtrsim 500 M_{\odot} \text{ yr}^{-1}$ following Barger et al. (2014). In Figure 25(a), we show the SFR density history computed for the redshift intervals $z = 1 - 2$, $2 - 3$, $3 - 4$, $4 - 5$, and $5 - 6$ (red circles). Below a redshift of $z \sim 2$, the SCUBA-2 contribution drops rapidly. Above $z \sim 2$, this SFR density history corresponds to $\sim 40\%$ (red curve) of the total SFR density history compiled by Madau & Dickinson (2014), after converting theirs to a Kroupa IMF (blue curve). Note, however, that we show our results for our adopted conversion from $L_{8-1000 \mu\text{m}}$ to SFR. Since Madau & Dickinson adopted a slightly lower conversion (see Section 3.1), we also need to apply that correction in order to do a proper comparison. That correction reduces the percentage from $\sim 40\%$ to $\sim 29\%$. (Although the present SFR density history is consistent with that found by Barger et al. 2014 using a subset of the current SCUBA-2 sample, in that paper we compared with the Hopkins & Beacom 2006 compilation, which is higher than the Madau & Dickinson

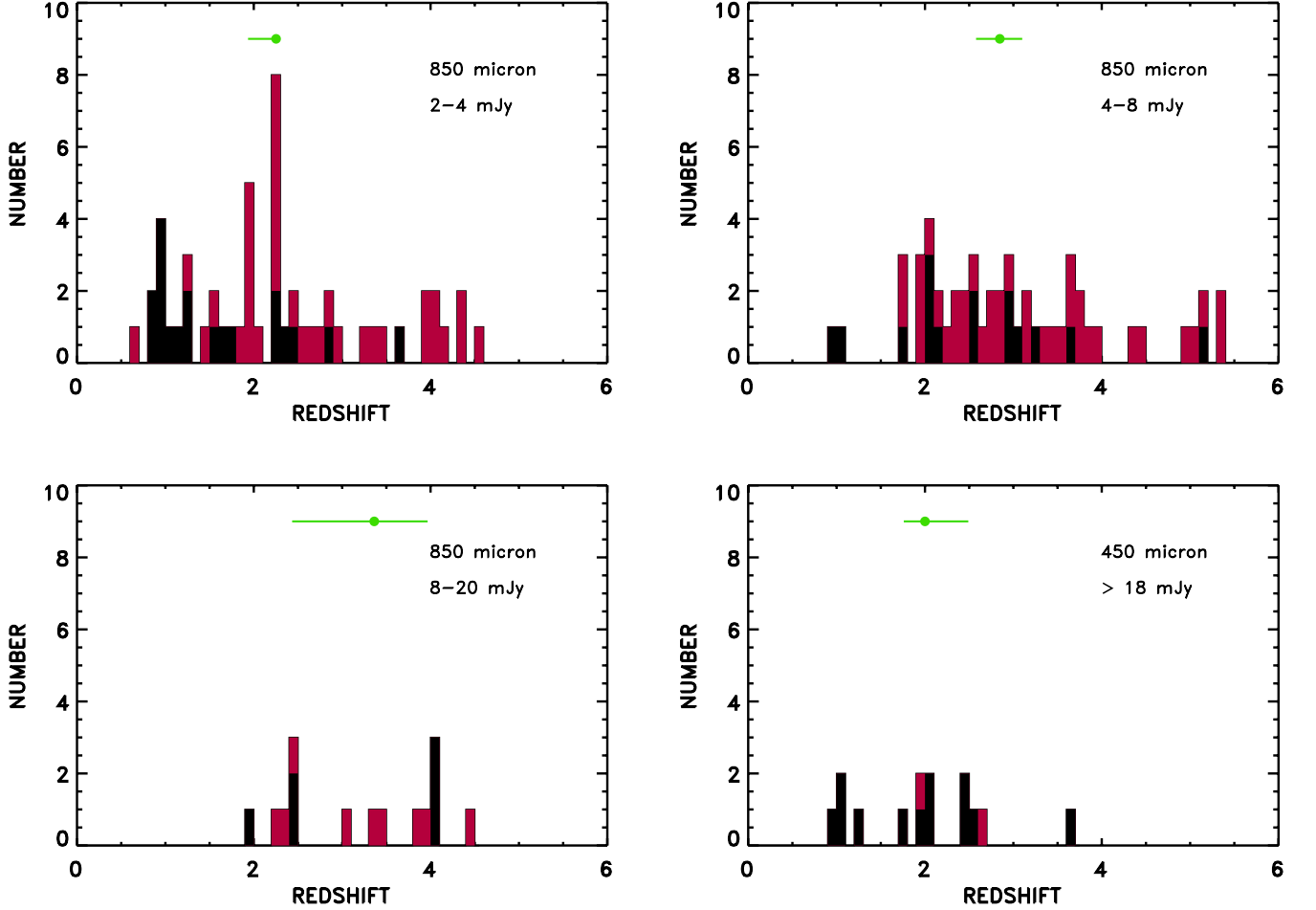


Figure 23. Redshift distributions for three intervals of 850 μm flux: (a) 2–4 mJy, (b) 4–8 mJy, and (c) 8–20 mJy, as well as for (d) the full 450 μm sample > 18 mJy. For each flux interval, sources are only shown if they lie in areas where the errors are low enough that all 4σ sources down to the flux limit are included (i.e., a complete sample). Black shows spectroscopic or photometric redshifts, and red shows z_{250} redshifts. The green circle shows the median redshift, and the green bar the 68% confidence interval on the median.

compilation. Thus, the contribution to the total that we quoted there was a lower 16%.) Clearly, the contribution of dusty, powerfully star-forming galaxies to the overall star formation history is impressively large.

The error bars in Figure 25(a) are purely statistical. However, systematic errors in the SFR conversion and in the redshift estimates may also be important. In order to estimate these potential errors, we recomputed the SFR density history randomly, reassigning the SFRs and redshifts within the potential error ranges. Based on these Monte Carlo calculations, we computed the 68% error range produced by the systematics, which we show as the red shaded region. For the highest and lowest redshifts, where there are fewer objects, the systematic and statistical errors are similar, but for redshifts between 2 and 4, the systematic error dominates.

In Figure 25(b), we show the SCUBA-2 SFR density distribution functions computed for the same redshift intervals vs. log SFR. Although the normalizations of the distribution functions are changing—they rise to reach a peak at $z = 2 - 3$ before dropping at higher redshifts—the shapes over $z = 2 - 5$ are remarkably similar; that is, the number density of high SFR galaxies relative to that of lower SFR galaxies is about the same in each redshift interval. However, at some point this similarity in shape must break down, as there cannot be large numbers of powerfully star-forming galaxies at very high redshifts. The present data show that this must occur at redshifts higher than $z \sim 5$.

In Figure 26, we show the SCUBA-2 distribution functions of Figure 25(b) recomputed for the coarser redshift

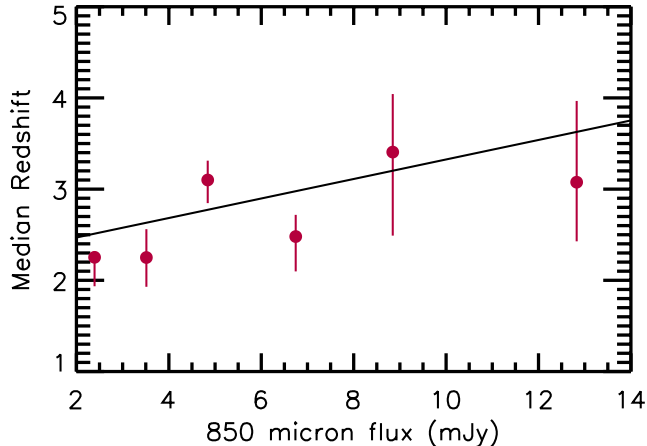


Figure 24. Median redshift vs. $850\,\mu\text{m}$ flux (red circles). The error bars show the 68% confidence intervals on the medians. The black line shows a linear least squares fit (Equation 7).

intervals $z = 1.25 - 2$, $2 - 4$, and $4 - 6$ (colored circles; note that in the $z = 4 - 6$ interval, there are not enough sources to plot the two highest SFR bins). We compare these with those computed at lower SFRs from the extinction-corrected UV samples of Reddy & Steidel (2009) and van der Burg et al. (2010) (small colored symbols and curves), assuming a Kennicutt (1998) conversion of UV luminosity to SFR for a Kroupa (2001) IMF. This emphasizes the disjoint nature of the SFRs of galaxies selected by UV and submillimeter observations (e.g., Barger et al. 2014): only submillimeter observations can find the most powerfully star-forming galaxies at redshifts $z \gtrsim 1$. Both the UV and SCUBA-2 distribution functions have similar shapes in the $z = 2 - 5$ interval. Thus, the number density of high SFR galaxies measured from the SCUBA-2 sample relative to that of lower SFR galaxies from UV-selected samples is about the same in this redshift interval. However, the normalizations of the SCUBA-2 functions appear slightly high relative to the UV functions at the overlap point. This may suggest that even at these lower SFRs, the UV samples are missing some star-forming galaxies.

4. SUMMARY

In this paper, we presented $\geq 4\sigma$ $850\,\mu\text{m}$ and $450\,\mu\text{m}$ catalogs from our uniform and deep SCUBA-2 survey of the GOODS-N/CANDELS/CDF-N field. We used submillimeter interferometry and 20 cm data to identify counterparts to the SCUBA-2 sources, which resulted in the localization of 114 of the 186 $850\,\mu\text{m}$ sources, including 26 of the 29 sources with $850\,\mu\text{m}$ fluxes above 6 mJy.

We obtained new spectroscopic redshifts with Keck and utilized spectroscopic and photometric redshifts from the literature, where possible. We also estimated redshifts from the 20 cm to $850\,\mu\text{m}$ flux ratio (millimetric redshifts) and from the $250\,\mu\text{m}$ to $850\,\mu\text{m}$ flux ratio (z_{250} redshifts). The redshift distribution of the submillimeter sample increases with both flux and wavelength, consistent with recent model predictions (Béthermin et al. 2015). We parameterized this dependence on flux. We showed how z_{250} is good enough (and better than millimetric) when compared with the spectroscopic redshifts for determining the SFR density history and the SFR density distribution functions for the SCUBA-2 sources with SFRs $\gtrsim 500 M_{\odot} \text{ yr}^{-1}$ for a Kroupa (2001) IMF.

We found that above $z \sim 2$, the contribution from the SCUBA-2 sources is an impressively large 29% of the total SFR density history compiled by Madau & Dickinson (2014). However, below $z \sim 2$, the SCUBA-2 contribution drops rapidly. We computed the SCUBA-2 SFR density distribution functions for five redshift intervals and found that, although the normalizations rise to a peak around $z = 2 - 3$ before dropping at higher redshifts, the shapes over $z = 2 - 5$ remain strikingly invariant. In other words, the number of high SFR galaxies relative to the number of lower SFR galaxies remains about the same in each redshift interval above $z \sim 2$. This shape invariance cannot be maintained to the highest redshifts, as eventually powerfully star-forming galaxies must disappear. We will investigate this further in a later paper in the series, where we will use the combined GOODS-N and GOODS-S datasets along with wider field samples.

We also compared the SCUBA-2 SFR density distribution functions in coarser redshift bins with results from extinction-corrected UV samples. As previously shown by Barger et al. (2014), the UV and submillimeter selected

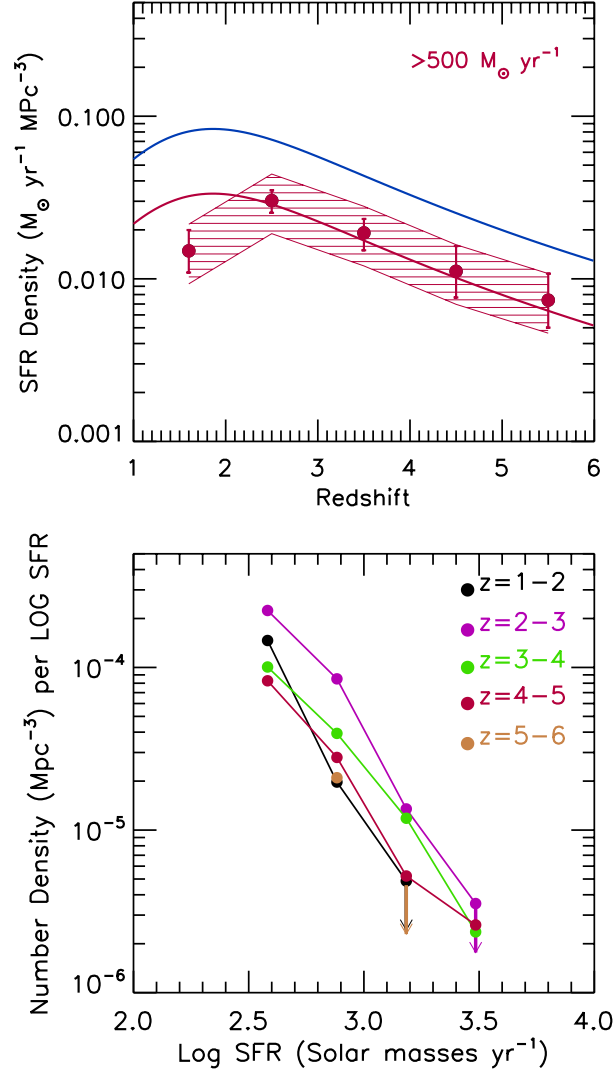


Figure 25. (a) SFR density per unit comoving volume vs. redshift for the SCUBA-2 sources with $\text{SFRs} \gtrsim 500 M_{\odot} \text{ yr}^{-1}$ for a Kroupa (2001) IMF (red circles; the 1σ error bars are Poissonian based on the number of sources in each bin). The computations were made at $z = 1-2$, $2-3$, $3-4$, $4-5$, and $5-6$ and are plotted at the mean redshift of each bin. The blue curve shows the SFR density history computed by Madau & Dickinson (2014), after we converted it to a Kroupa IMF, and the red curve shows it multiplied by 0.4 to match roughly the SFR density history of the SCUBA-2 sources. However, once we also take into account the different FIR calibrations that were used in this work versus in Madau & Dickinson, we find that the SCUBA-2 data are only 0.29 times the Madau & Dickinson curve. The red shaded region shows the 68% confidence range when allowance is made for the systematic uncertainties in the SFR calibrations. (b) Number density per unit comoving volume per unit log SFR vs. log SFR in five redshift intervals (see legend).

samples are nearly disjoint, with only the submillimeter observations able to find the most powerfully star-forming galaxies in the universe. We found that at both wavelengths, the shapes of the distribution functions are similar from $z = 2-5$; however, the normalizations of the SCUBA-2 functions are slightly high relative to the UV functions in the overlap region. This may suggest that the UV samples are still missing some star-forming galaxies, even at these lower SFRs. However, it may also simply be due to uncertain extinction corrections in the UV and different calibrations of the SFRs in the two populations.

We thank the referee for a very useful report that improved the paper. We gratefully acknowledge support from NSF grants AST-0709356 (L. L. C., L.-Y. H.) and AST-1313150 (A. J. B.), the John Simon Guggenheim Memorial Foundation and Trustees of the William F. Vilas Estate (A. J. B.), and the ERC Advanced Investigator programme DUSTYGAL 321334 (C.-C. C.). The James Clerk Maxwell Telescope has historically been operated by the Joint Astronomy Centre on behalf of the Science and Technology Facilities Council of the United Kingdom, the National

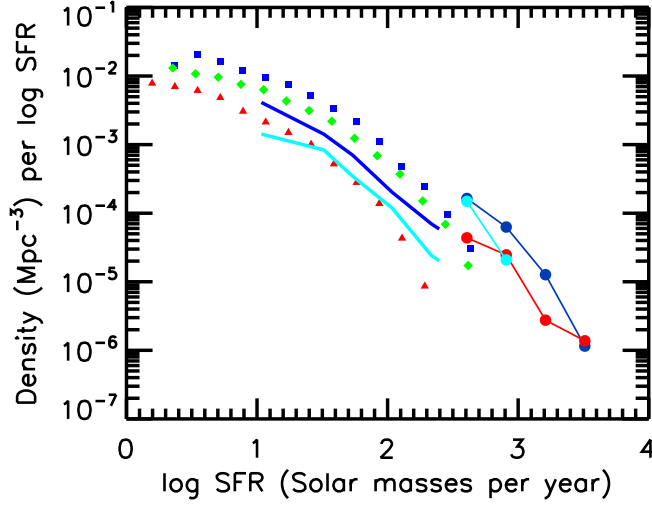


Figure 26. Number density per unit comoving volume per unit log SFR vs. log SFR from Figure 25, but now in three coarser redshift intervals (circles: red— $z = 1.25 - 2$; blue— $z = 2 - 4$; cyan— $z = 4 - 6$). For comparison, the small symbols and curves show extinction-corrected UV results from Reddy & Steidel (2009; cyan curve— $z \sim 3$, blue curve— $z \sim 2$) and van der Burg (2010; red triangles— $z = 4.8$, green diamonds— $z = 3.8$, blue squares— $z = 3.1$), assuming a Kennicutt (1998) conversion of UV luminosity to SFR for a Kroupa (2001) IMF. The higher van der Burg et al. than Reddy & Steidel values reflect their larger adopted extinction corrections.

Research Council of Canada and the Netherlands Organisation for Scientific Research. Additional funds for the construction of SCUBA-2 were provided by the Canada Foundation for Innovation. We acknowledge the cultural significance that the summit of Maunakea has to the indigenous Hawaiian community.

REFERENCES

- Alexander, D. M., Bauer, F. E., Brandt, W. N., et al. 2003, *AJ*, 126, 539
- Aravena, M., Decarli, R., Walter, F., et al. 2016, *ApJ*, 833, 68
- Barger, A. J., Cowie, L. L., Chen, C.-C., et al. 2014, *ApJ*, 784, 9
- Barger, A. J., Cowie, L. L., Owen, F. N., et al. 2015, *ApJ*, 801, 87
- Barger, A. J., Cowie, L. L., Owen, F. N., Hsu, L.-Y., Wang, W.-H. 2017, *ApJ*, 835, 95
- Barger, A. J., Cowie, L. L., & Wang, W.-H. 2008, *ApJ*, 689, 687
- Barger, A. J., Cowie, L. L., & Richards, E. A. 2000, *AJ*, 119, 2092
- Barger, A. J., Cowie, L. L., Sanders, D. B., et al. 1998, *Nature*, 394, 248
- Barger, A. J., Wang, W.-H., Cowie, L. L., et al. 2012, *ApJ*, 761, 89
- B  thermin, M., De Breuck, C., Sargent, M., & Daddi, E. 2014, *A&A*, 576, L9
- Blain, A. W., Kneib, J.-P., Ivison, R. J., & Smail, I. 1999, *ApJ*, 512, L87
- Blain, A. W., Smail, I., Ivison, R. J., Kneib, J.-P., & Frayer, D. T. 2002, *PhR*, 369, 111
- Bothwell, M. S., Smail, I., Chapman, S. C., et al. 2013, *MNRAS*, 429, 3047
- Bouwens, R., Aravena, M., Decarli, R., et al. 2016, *ApJ*, 833, 72
- Briggs, D. S. 1995, *BAAS*, 27, 1444
- Caputi, K. I., Dunlop, J. S., McLure, R. J., et al. 2012, *ApJ*, 750, L20
- Carilli, C. L., & Yun, M. S. 1999, *ApJ*, 513, L13
- Casey, C. M. 2012, *MNRAS*, 425, 3094
- Casey, C. M., Chen, C.-C., Cowie, L. L., et al. 2013, *MNRAS*, 436, 1919
- Casey, C. M., Narayanan, D., & Cooray, A. 2014, *PhR*, 541, 45
- Chabrier, G. 2003, *PASP*, 115, 763
- Chakrabarti, S., Magnelli, B., McKee, C. F., et al. 2013, *ApJ*, 773, 113
- Chapin, E. L., Berry, D. S., Gibb, A. G., et al. 2013, *MNRAS*, 430, 2545
- Chapman, S. C., Barger, A. J., Cowie, L. L., et al. 2003, *ApJ*, 585, 57
- Chapman, S. C., Blain, A., Ibata, R., et al. 2009, *ApJ*, 691, 560
- Chapman, S. C., Blain, A. W., Smail, I., & Ivison, R. J. 2005, *ApJ*, 622, 772
- Chen, C.-C., Cowie, L. L., Barger, A. J., et al. 2013a, *ApJ*, 762, 81
- Chen, C.-C., Cowie, L. L., Barger, A. J., et al. 2013b, *ApJ*, 776, 131
- Chen, C.-C., Smail, I., Ivison, R. J., et al. 2016, *ApJ*, 820, 82
- Chen, C.-C., Smail, I., Swinbank, A. M., et al. 2015, *ApJ*, 799, 194
- Cohen, J. G., Hogg, D. W., Blandford, R., et al. 2000, *ApJ*, 538, 29
- Condon, J. J. 1992, *ARA&A*, 30, 575
- Cooper, M. C., Aird, J. A., Coil, A. L., et al. 2011, *ApJS*, 193, 14
- Cowie, L. L., Barger, A. J., Hu, E. M., Capak, P., & Songaila, A. 2004, *AJ*, 127, 3137
- Cowie, L. L., Barger, A. J., & Kneib, J.-P. 2002, *AJ*, 123, 2197
- Cowie, L. L., Barger, A. J., & Songaila, A. 2016, *ApJ*, 817, 57
- Cowie, L. L., Songaila, A., Hu, E. M., & Cohen, J. G. 1996, *AJ*, 112, 839
- da Cunha, E., Walter, F., Smail, I. R., et al. 2015, *ApJ*, 806, 110
- Daddi, E., Dannerbauer, H., Krips, M., et al. 2009a, *ApJ*, 695, L176
- Daddi, E., Dannerbauer, H., Stern, D., et al. 2009b, *ApJ*, 694, 1517
- Dempsey, J. T., Friberg, P., Jenness, T., et al. 2013, *MNRAS*, 430, 2534
- Dunlop, J. S., McLure, R. J., Biggs, A. D., et al. 2017, *MNRAS*, 466, 861
- Eales, S., Lilly, S., Gear, W., et al. 1999, *ApJ*, 515, 518
- Elbaz, D., Dickinson, M., Hwang, H. S., et al. 2011, *A&A*, 533, A119
- Fritz, J., Franceschini, A., & Hatziminaoglou, E. 2006, *MNRAS*, 366, 767
- Fujimoto, S., Ouchi, M., Ono, Y., et al. 2016, *ApJS*, 222, 1
- Geach, J. E., Chapin, E. L., Coppin, K. E. K., et al. 2013, *MNRAS*, 432, 53
- Geach, J. E., Dunlop, J. S., Halpern, M., et al. 2017, *MNRAS*, 465, 1789

- Giavalisco, M., Dickinson, M., Ferguson, H. C., et al. 2004, *ApJL*, 600, L93
- González-López, J., Bauer, F. E., Romero-Cañizales, C., et al. 2016, *A&A*, 597, 41
- Grogin, N. A., Kocevski, D. D., Faber, S. M., et al. 2011, *ApJS*, 197, 35
- Gruppioni, C., Pozzi, F., Rodighiero, G., et al. 2013, *MNRAS*, 432, 23
- Ho, P. T. P., Moran, J. M., & Lo, K. Y. 2004, *ApJ*, 616, L1
- Hodge, J. A., Karim, A., Smail, I., et al. 2013, *ApJ*, 768, 91
- Hodge, J. A., Riechers, D., Decarli, R., et al. 2015, *ApJL*, 798, L18
- Holland, W. S., Bintley, D., Chapin, E. L., et al. 2013, *MNRAS*, 430, 2513
- Holland, W. S., Robson, E. I., Gear, W. K., et al. 1999, *MNRAS*, 303, 659
- Hönig, S. F., & Kishimoto, M. 2010, *A&A*, 523, 27
- Hopkins, A. M., & Beacom, J. F. 2006, *ApJ*, 651, 142
- Hsu, L.-Y., Cowie, L. L., Chen, C.-C., Barger, A. J., & Wang, W.-H. 2016, *ApJ*, 829, 25
- Hughes, D. H., Serjeant, S., Dunlop, J., et al. 1998, *Nature*, 394, 241
- Ivion, R. J., Greve, T. R., Smail, I., et al. 2002, *MNRAS*, 337, 1
- Jenness, T., Berry, D., Chapin, E., et al. 2011, in *ASP Conf. Ser.* 442, *Astronomical Data Analysis Software and Systems XX*, ed. I. N. Evans, A. Accomazzi, D. J. Mink, & A. H. Rots (San Francisco, CA: ASP), 281
- Jenness, T., Cavanagh, B., Economou, F., & Berry, D. S. 2008, in *ASP Conf. Ser.* 394, *Astronomical Data Analysis Software and Systems XVII*, ed. R. W. Argyle, P. S. Bunclark, & J. R. Lewis (San Francisco, CA: ASP), 565
- Karim, A., Swinbank, A. M., Hodge, J. A., et al. 2013, *MNRAS*, 432, 2
- Koekemoer, A. M., Faber, S. M., Ferguson, H. C., et al. 2011, *ApJS*, 197, 36
- Kroupa, P. 2001, *MNRAS*, 322, 231
- Knudsen, K. K., van der Werf, P. P., & Kneib, J.-P. 2008, *MNRAS*, 384, 1611
- Larson, D., Dunkley, J., Hinshaw, G., et al. 2011, *ApJS*, 192, 16
- Leitherer, C., Schaerer, D., Goldader, J. D., et al. 1999, *ApJS*, 123, 3
- Le Floc'h, E., Papovich, C., Dole, H., et al. 2005, *ApJ*, 632, 169
- Lutz, D., Poglitsch, A., Altieri, B., et al. 2011, *A&A*, 532, A90
- Madau, P., & Dickinson, M., 2014, *ARA&A*, 52, 415
- Magnelli, B., Popesso, P., Berta, S., et al. 2013, *A&A*, 553, A132
- Miettinen, O., Smolčić, V., Novak, M., et al. 2015, *A&A*, 577, A29
- Momcheva, I. G., Brammer, G. B., van Dokkum, P. G., et al. 2016, *ApJS*, 225, 27
- Morrison, G. E., Owen, F. N., Dickinson, M., Ivison, R. J., & Ibar, E. 2010, *ApJS*, 188, 178
- Mullaney, J. R., Alexander, D. M., Goulding, A. D., & Hickox, R. C. 2011, *MNRAS*, 414, 1082
- Murphy, E. J., Condon, J. J., Schinnerer, E., et al. 2011, *ApJ*, 737, 67
- Netzer, H., Lutz, D., Schweitzer, M., et al. 2007, *ApJ*, 666, 806
- Oliver, S., Bock, J., Altieri, B., et al. 2012, *MNRAS*, 424, 1614
- Oteo, I., Zwaan, M. A., Ivison, R. J., Smail, I., & Biggs, A. D. 2016, *ApJ*, 822, 36
- Penner, K., Pope, A., Chapin, E. L., et al. 2011, *MNRAS*, 410, 2749
- Pope, A., Borys, C., Scott, D., et al. 2005, *MNRAS*, 358, 149
- Pope, A., Chary, R.-R., Alexander, D. M., et al. 2008, *ApJ*, 675, 1171
- Rafferty, D. A., Brandt, W. N., Alexander, D. M., et al. 2011, *ApJ*, 742, 3
- Reddy, N. A., Dickinson, M., Elbaz, D., et al. 2012, *ApJ*, 744, 154
- Reddy, N. A., & Steidel, C. C. 2009, *ApJ*, 692, 778
- Reddy, N. A., Steidel, C. C., Erb, D. K., Shapley, A. E., & Pettini, M. 2006, *ApJ*, 653, 1004
- Richards, E. A. 2000, *ApJ*, 533, 611
- Salpeter, E. E. 1955, *ApJ*, 121, 161
- Schartmann, M., Meisenheimer, K., Camenzind, M., et al. 2008, *A&A*, 482, 67
- Serjeant, S., Dunlop, J. S., Mann, R. G., et al. 2003, *MNRAS*, 344, 887
- Shu, X. W., Elbaz, D., Bourne, N., et al. 2016, *ApJS*, 222, 4
- Siebenmorgen, R., Heymann, F., & Efstathiou, A. 2015, *A&A*, 583, 120
- Silva, L., Granato, G. L., Bressan, A., & Danese, L. 1998, *ApJ*, 509, 103
- Simpson, J. M., Smail, I., Swinbank, A. M., et al. 2015, *ApJ*, 807, 128
- Smail, I., Ivison, R. J., & Blain, A. W. 1997, *ApJ*, 490, L5
- Smolčić, V., Aravena, M., Navarrete, F., et al. 2012, *A&A*, 548, 4
- Staguhn, J., G., Kovács, A., Arendt, R. G., et al. 2014, *ApJ*, 790, 77
- Swinbank, A. M., Simpson, J. M., Smail, I., et al. 2014, *MNRAS*, 438, 1267
- Swinbank, A. M., Smail, I., Chapman, S. C., et al. 2004, *ApJ*, 617, 64
- Treu, T., Ellis, R. S., Liao, T. X., et al. 2005, *ApJ*, 622, L5
- Trouille, L., Barger, A. J., Cowie, L. L., Yang, Y., & Mushotzky, R. F. 2008, *ApJ*, 179, 1
- van der Burg, R. F. J., Hildebrandt, H., & Erben, T. 2010, *A&A*, 523, A74
- Walter, F., Decarli, R., Carilli, C., et al. 2012, *Nature*, 486, 233
- Wang, T., Elbaz, D., Schreiber, C., et al. 2016, *ApJ*, 816, 84
- Wang, W.-H., Barger, A. J., & Cowie, L. L. 2012, *ApJ*, 744, 155
- Wang, W.-H., Cowie, L. L., & Barger, A. J. 2004, *ApJ*, 613, 655
- Wang, W.-H., Cowie, L. L., Barger, A. J., Keenan, R. C., & Ting, H.-C. 2010, *ApJS*, 187, 251
- Wang, W.-H., Cowie, L. L., Barger, A. J., & Williams, J. P. 2011, *ApJ*, 726, L18
- Wardlow, J. L., Smail, I., Coppin, K. E. K., et al. 2011, *MNRAS*, 415, 1479
- Wirth, G. D., Trump, J. R., Barro, G., et al. 2015, *AJ*, 150, 153
- Wirth, G. D., Willmer, C. N. A., Amico, P., et al. 2004, *AJ*, 127, 3121
- Yamaguchi, Y., Tamura, Y., Kohno, K., et al. 2016, *PASJ*, 68, 82
- Younger, J. D., Fazio, G. G., Wilner, D. J., et al. 2008, *ApJ*, 688, 59

Table 5. SCUBA-2 850 Micron Sample (4σ)

No.	Name	R.A. (SCUBA-2) (J2000.0)	Decl. (J2000.0)	Flux (mJy)	Error (mJy)	S/N	R.A. (accurate) (J2000.0)	Decl. (J2000.0)	SMA (mJy)	20 cm (μ Jy)	K_s (AB)	z	z_{250}
(1)	(2)	(3)	(4)	(5)	(6)	(7)	(8)	(9)	(10)	(11)	(12)	(13)	(14)
1	SMM123551622145	12 35 51.71	62 21 45.2	19.6	1.49	13.1	12 35 51.37	62 21 47.2	13.7	51	22.1	...	3.96
2	SMM123712622210	12 37 12.05	62 22 10.9	17.3	0.94	18.4	12 37 11.92	62 22 12.0	23.9	87	22.4	4.055 f _{1,g}	4.12
3	SMM123730621258	12 37 30.69	62 12 58.6	13.4	0.39	33.7	12 37 30.80	62 12 58.7	14.9	126	22.9	2.43	2.46
4	SMM123555622238	12 35 55.85	62 22 38.2	12.8	1.72	7.4	12 35 55.88	62 22 39.0	17.0	56	22.1	...	3.07
5	SMM123546622012	12 35 46.87	62 20 12.0	11.9	1.21	9.8	12 35 46.64	62 20 13.3	14.0	46	22.7	...	2.26
6	SMM123623620334	12 36 23.76	62 03 34.7	11.9	1.18	10.1	2.42
7	SMM123627620605	12 36 27.28	62 06 5.89	11.2	0.80	14.0	12 36 27.21	62 06 5.50	11.5	34	24.8	...	4.47
8	SMM123633621407	12 36 33.46	62 14 7.91	9.4	0.36	26.0	12 36 33.42	62 14 8.50	12.0	33	25.5	4.042 f ₂	4.40
9	SMM123817620900	12 38 17.69	62 09 0.29	9.0	1.32	6.8	12 38 18.21	62 08 58.0	...	105	21.5	...	2.32
10	SMM123709622200	12 37 9.320	62 22 0.89	9.0	0.90	9.9	12 37 8.822	62 22 1.90	9.2	143	23.7	4.051 f ₁	3.76
11	SMM123549621905	12 35 49.07	62 19 5.09	8.8	1.01	8.7	12 35 48.84	62 19 4.91	...	71	22.8	...	3.36
12	SMM123550621041	12 35 50.51	62 10 41.2	8.6	0.80	10.8	12 35 50.35	62 10 41.9	10.1	25	23.4	...	3.40
13	SMM123711621329	12 37 11.53	62 13 29.9	8.5	0.34	24.9	12 37 11.34	62 13 30.9	6.7	123	20.4	1.995 d _{1,g}	1.98
14	SMM123631621712	12 36 31.99	62 17 12.9	8.4	0.40	20.9	12 36 31.94	62 17 14.7	7.1	21	23.0	...	3.89
15	SMM123707621408	12 37 7.390	62 14 8.89	8.3	0.33	25.2	12 37 7.177	62 14 8.19	7.1	58	21.4	2.490 d _{1,g}	2.83
16	SMM123629620255	12 36 29.30	62 02 55.9	7.8	1.29	6.0	12 36 29.21	62 02 53.9	...	213	21.1	...	2.48
17	SMM123515621510	12 35 15.27	62 15 10.9	7.4	1.71	4.3	12 35 14.91	62 15 9.99	...	237	22.1	...	2.33
18	SMM123618621549	12 36 18.54	62 15 49.7	7.3	0.42	17.4	12 36 18.35	62 15 50.4	7.2	163	22.0	2.000 e _{1,g}	2.00
19	SMM123553621338	12 35 53.84	62 13 38.3	7.1	0.73	9.7	12 35 53.26	62 13 37.5	4.3	41	22.8	2.098 c	2.23
20	SMM123634621921	12 36 34.84	62 19 21.9	6.9	0.70	9.8	12 36 34.92	62 19 23.5	8.9	85	21.7	...	2.41
21	SMM123721620709	12 37 21.29	62 07 9.79	6.7	0.74	9.0	12 37 21.40	62 07 8.30	...	294	20.9	...	1.97
22	SMM123722620539	12 37 22.97	62 05 39.7	6.7	0.87	7.7	12 37 23.00	62 05 39.5	...	71	22.1	...	2.62
23	SMM123638620226	12 36 38.55	62 02 26.9	6.6	1.37	4.8	< 12	1.64
24	SMM123644621938	12 36 44.75	62 19 38.9	6.6	0.69	9.5	< 12	3.98
25	SMM123701621145	12 37 1.501	62 11 45.9	6.5	0.32	20.2	12 37 1.578	62 11 46.4	4.8	95	20.5	1.760 e	2.04
26	SMM123652621224	12 36 52.07	62 12 24.9	6.3	0.29	21.4	12 36 52.03	62 12 25.9	7.8	12	99.0	5.183 h	5.51
27	SMM123539621241	12 35 39.71	62 12 41.7	6.2	0.88	7.0	12 35 39.58	62 12 44.0	...	22	22.6	...	3.61
28	SMM123812621453	12 38 12.39	62 14 53.5	6.1	0.97	6.3	12 38 12.45	62 14 55.3	...	44	19.4	...	2.71
29	SMM123632620621	12 36 32.98	62 06 21.9	6.0	0.76	7.9	12 36 32.69	62 06 21.1	...	33	23.8	...	3.71
30	SMM123803620631	12 38 3.468	62 06 31.7	5.9	1.28	4.6	< 12	5.05
31	SMM123646621447	12 36 46.05	62 14 47.9	5.9	0.32	18.5	12 36 46.08	62 14 48.6	4.2	101	22.4	3.63	2.34
32	SMM123616620701	12 36 16.71	62 07 1.69	5.9	0.77	7.7	12 36 16.54	62 07 2.79	...	26	21.6	...	2.49
33	SMM123617622315	12 36 17.54	62 23 15.7	5.9	1.35	4.3	< 12	3.72
34	SMM123714621824	12 37 14.02	62 18 24.9	5.9	0.46	12.7	12 37 13.89	62 18 26.2	...	625	24.4	...	3.44
35	SMM123741621221	12 37 41.10	62 12 21.4	5.8	0.47	12.2	12 37 41.16	62 12 21.0	7.1	27	23.3	3.02	2.55
36	SMM123610620646	12 36 10.01	62 06 46.5	5.8	0.84	6.9	2.84
37	SMM123633620257	12 36 33.85	62 02 57.9	5.6	1.24	4.5	< 12	5.35
38	SMM123738621731	12 37 38.10	62 17 31.5	5.6	0.71	7.8	12 37 38.09	62 17 32.2	...	19	24.5	...	5.34
39	SMM123539621308	12 35 39.70	62 13 8.79	5.5	0.88	6.3	12 35 39.49	62 13 11.0	8.5	35	24.0	...	5.34
40	SMM123648622104	12 36 48.33	62 21 4.00	5.5	0.79	6.9	12 36 48.29	62 21 6.99	...	41	22.6	...	4.48
41	SMM123610622043	12 36 10.12	62 20 43.5	5.5	0.93	5.9	1.72
42	SMM123622621620	12 36 22.26	62 16 20.7	5.4	0.41	12.9	< 12	2.56
43	SMM123616621514	12 36 16.12	62 15 14.7	5.4	0.42	12.8	12 36 16.10	62 15 13.7	3.4	36	22.2	2.578 c	2.12
44	SMM123553620930	12 35 53.26	62 09 30.2	5.3	0.81	6.5	12 35 53.03	62 09 29.5	...	41	22.9	...	3.72
45	SMM123636620708	12 36 36.25	62 07 8.90	5.3	0.56	9.3	12 36 35.89	62 07 7.50	...	61	19.3	0.9500 a ₁	1.67
46	SMM123528621428	12 35 28.61	62 14 28.4	5.2	1.10	4.7	< 12	5.23

Table 5 continued on next page

Table 5 (*continued*)

No.	Name	R.A. (SCUBA-2) (J2000.0)	Decl. (J2000.0)	Flux (mJy)	Error (mJy)	S/N	R.A. (accurate) (J2000.0)	Decl. (J2000.0)	SMA (mJy)	20 cm (μ Jy)	K_s (AB)	z	z_{250}
(1)	(2)	(3)	(4)	(5)	(6)	(7)	(8)	(9)	(10)	(11)	(12)	(13)	(14)
47	SMM123620620637	12 36 20.71	62 06 37.8	5.2	0.78	6.6	12 36 20.47	62 06 39.6	...	42	21.5	...	2.84
48	SMM123803620840	12 38 3.980	62 08 40.7	5.1	1.02	5.0	< 12	4.75
49	SMM123635621424	12 36 35.76	62 14 24.9	4.9	0.35	13.9	12 36 35.59	62 14 24.0	...	82	20.1	2.005 a2,c	1.99
50	SMM123645622019	12 36 45.32	62 20 19.0	4.9	0.75	6.5	12 36 45.30	62 20 19.7	...	27	23.6	...	3.60
51	SMM123621621706	12 36 21.25	62 17 6.79	4.9	0.44	11.0	12 36 21.28	62 17 8.40	3.4	164	21.9	...	2.17
52	SMM123651620500	12 36 51.64	62 05 0.99	4.8	0.86	5.6	12 36 51.71	62 05 3.00	...	79	24.0	...	3.19
53	SMM123712621035	12 37 12.64	62 10 35.9	4.8	0.39	12.2	12 37 12.48	62 10 35.6	...	23	23.5	...	3.10
54	SMM123726620822	12 37 26.73	62 08 22.7	4.8	0.55	8.7	12 37 26.66	62 08 23.2	...	52	21.2	2.59	2.47
55	SMM123627621218	12 36 27.61	62 12 18.9	4.8	0.37	12.9	12 36 27.55	62 12 18.0	...	17	24.7	...	5.12
56	SMM123542620826	12 35 42.73	62 08 26.9	4.7	1.01	4.6	< 12	4.41
57	SMM123719621218	12 37 19.37	62 12 18.8	4.6	0.38	12.1	12 37 18.96	62 12 17.5	...	16	23.1	...	3.88
58	SMM123743620752	12 37 43.97	62 07 52.4	4.6	0.83	5.5	12 37 44.11	62 07 54.0	...	39	23.1	...	2.39
59	SMM123617621929	12 36 17.47	62 19 29.7	4.6	0.78	5.9	12 36 17.05	62 19 31.9	...	60	21.6	...	2.22
60	SMM123802621853	12 38 2.808	62 18 53.9	4.5	1.04	4.3	< 12	5.03
61	SMM123634620529	12 36 34.69	62 05 29.9	4.5	0.83	5.4	< 12	5.02
62	SMM123637620853	12 36 37.22	62 08 53.0	4.4	0.42	10.4	12 36 37.03	62 08 52.4	...	79	22.0	2.13	2.58
63	SMM123629621045	12 36 29.21	62 10 45.8	4.4	0.40	11.0	12 36 29.03	62 10 45.5	7.7	48	19.7	1.013 a1,c	1.77
64	SMM123636621156	12 36 36.92	62 11 56.9	4.4	0.35	12.4	< 12	1.95
65	SMM123658620932	12 36 58.64	62 09 32.0	4.4	0.38	11.4	12 36 58.55	62 09 31.4	4.6	27	23.5	...	2.95
66	SMM123800621616	12 38 0.128	62 16 16.9	4.4	0.84	5.2	2.19
67	SMM123620620551	12 36 20.15	62 05 51.7	4.3	0.86	5.0	< 12	4.98
68	SMM123814621422	12 38 14.37	62 14 22.4	4.3	0.99	4.3	< 12	2.00
69	SMM123655620418	12 36 55.34	62 04 18.0	4.3	0.94	4.5	12 36 55.42	62 04 18.0	...	56	22.9	...	2.29
70	SMM123540621439	12 35 40.07	62 14 39.9	4.2	0.89	4.7	12 35 39.96	62 14 42.0	...	79	22.8	2.93	1.73
71	SMM123807621046	12 38 7.210	62 10 46.6	4.1	0.94	4.3	< 12	3.54
72	SMM123734620527	12 37 34.37	62 05 27.5	4.1	0.97	4.2	< 12	4.36
73	SMM123702621426	12 37 2.658	62 14 26.9	4.0	0.31	12.8	12 37 2.600	62 14 26.9	...	18	22.2	3.214 a1,a3	2.78
74	SMM123808621425	12 38 8.942	62 14 25.7	4.0	0.90	4.4	< 12	2.31
75	SMM123728621920	12 37 28.39	62 19 20.7	4.0	0.75	5.4	12 37 28.12	62 19 20.1	...	26	24.0	...	2.77
76	SMM123643622058	12 36 43.73	62 20 58.0	4.0	0.79	5.0	3.31
77	SMM123712621211	12 37 12.09	62 12 11.9	4.0	0.36	11.0	12 37 12.05	62 12 11.9	5.3	33	22.0	2.914 c	2.81
78	SMM123658621451	12 36 58.65	62 14 51.0	3.9	0.32	12.4	< 12	1.99
79	SMM123542620956	12 35 42.96	62 09 56.9	3.9	0.90	4.3	12 35 43.12	62 09 55.4	...	66	22.1	...	1.79
80	SMM123656621205	12 36 56.35	62 12 5.00	3.9	0.30	13.0	12 36 56.59	62 12 7.40	...	42	25.0	...	3.75
81	SMM123801621302	12 38 1.442	62 13 2.89	3.9	0.81	4.8	12 38 1.856	62 13 0.90	...	44	21.0	1.11	2.09
82	SMM123605620836	12 36 5.841	62 08 36.4	3.8	0.75	5.1	12 36 5.621	62 08 37.7	...	19	22.7	...	4.81
83	SMM123623620520	12 36 23.15	62 05 20.8	3.8	0.90	4.2	< 12	4.79
84	SMM123659622211	12 36 59.26	62 22 11.9	3.8	0.91	4.1	12 36 58.96	62 22 15.4	...	27	22.8	...	2.13
85	SMM123608621438	12 36 8.408	62 14 38.5	3.6	0.45	8.0	12 36 8.598	62 14 35.4	...	41	22.6	...	2.81
86	SMM123634620940	12 36 34.80	62 09 40.9	3.6	0.41	8.7	< 12	3.49
87	SMM123540621217	12 35 40.86	62 12 17.9	3.6	0.87	4.1	12 35 40.71	62 12 18.9	...	71	22.1	...	1.81
88	SMM123709620839	12 37 9.909	62 08 39.9	3.6	0.43	8.3	0.967
89	SMM123550621538	12 35 50.05	62 15 38.2	3.6	0.80	4.5	< 12	1.99
90	SMM123631620958	12 36 31.21	62 09 58.9	3.5	0.41	8.6	12 36 31.26	62 09 57.6	...	148	21.7	2.313 a3	1.77
91	SMM123609620800	12 36 9.001	62 08 0.59	3.5	0.76	4.6	12 36 8.869	62 08 3.90	...	26	22.8	...	2.95
92	SMM123754621102	12 37 54.21	62 11 2.09	3.5	0.77	4.5	12 37 54.37	62 10 59.3	...	303	20.0	1.306 a1	2.39
93	SMM123701622024	12 37 1.842	62 20 24.0	3.5	0.75	4.6	12 37 1.560	62 20 24.7	...	60	22.1	3.49	2.66
94	SMM123652620643	12 36 52.21	62 06 43.9	3.5	0.70	4.9	< 12	2.56

Table 5 continued on next page

Table 5 (*continued*)

No.	Name	R.A. (SCUBA-2) (J2000.0)	Decl. (J2000.0)	Flux (mJy)	Error (mJy)	S/N	R.A. (accurate) (J2000.0)	Decl. (J2000.0)	SMA (mJy)	20 cm (μ Jy)	K_s (AB)	z	z_{250}
(1)	(2)	(3)	(4)	(5)	(6)	(7)	(8)	(9)	(10)	(11)	(12)	(13)	(14)
95	SMM123719621021	12 37 19.35	62 10 21.7	3.5	0.41	8.5	12 37 19.55	62 10 21.2	...	23	24.1	...	3.26
96	SMM123557621726	12 35 57.59	62 17 26.2	3.4	0.79	4.3	12 35 57.18	62 17 25.0	...	32	22.4	0.8263 a1	4.64
97	SMM123728621422	12 37 28.42	62 14 22.7	3.4	0.39	8.6	< 12	1.92
98	SMM123608620852	12 36 8.122	62 08 52.5	3.3	0.72	4.7	12 36 8.356	62 08 52.6	...	29	21.9	...	2.33
99	SMM123741621903	12 37 41.01	62 19 3.40	3.3	0.80	4.1	12 37 41.48	62 19 3.49	...	68	22.5	0.8805 a1	2.00
100	SMM123718620654	12 37 18.87	62 06 54.8	3.3	0.75	4.4	12 37 18.90	62 06 56.9	...	21	24.3	...	3.54
101	SMM123601621804	12 36 1.450	62 18 4.40	3.2	0.80	4.0	12 36 0.963	62 18 7.00	...	72	21.5	1.77	1.86
102	SMM123713621156	12 37 13.94	62 11 56.9	3.2	0.38	8.5	12 37 14.05	62 11 56.5	3.2	22	24.2	...	2.91
103	SMM123732620728	12 37 32.98	62 07 28.5	3.2	0.78	4.1	< 12	4.55
104	SMM123711621118	12 37 11.78	62 11 18.9	3.1	0.38	8.3	< 12	4.35
105	SMM123717620801	12 37 17.32	62 08 1.90	3.1	0.51	6.1	12 37 17.46	62 08 4.40	...	67	20.8	...	1.24
106	SMM123725620857	12 37 25.03	62 08 57.6	3.1	0.48	6.4	12 37 25.00	62 08 56.5	...	84	19.6	0.9367 a1	1.28
107	SMM123612620834	12 36 12.69	62 08 34.7	3.1	0.70	4.4	12 36 12.63	62 08 35.2	...	21	21.8	2.25	2.95
108	SMM123620621908	12 36 20.07	62 19 8.79	3.0	0.74	4.0	1.65
109	SMM123600621051	12 36 0.640	62 10 51.4	3.0	0.70	4.2	12 36 0.450	62 10 53.3	...	51	22.9	...	2.49
110	SMM123634621239	12 36 34.47	62 12 39.9	2.9	0.34	8.3	12 36 34.51	62 12 40.9	...	185	19.9	1.224 a1,g	0.686
111	SMM123650620822	12 36 50.21	62 08 22.0	2.8	0.42	6.6	2.57
112	SMM123700620910	12 37 0.058	62 09 10.0	2.8	0.39	7.2	12 37 0.270	62 09 9.70	3.1	297	21.8	...	1.99
113	SMM123723621713	12 37 23.76	62 17 13.7	2.7	0.44	6.3	12 37 23.56	62 17 13.7	...	26	23.8	...	2.67
114	SMM123703620755	12 37 3.907	62 07 55.9	2.7	0.46	5.9	12 37 4.108	62 07 55.0	...	64	19.4	1.253 a2	1.34
115	SMM123646620833	12 36 46.51	62 08 33.0	2.7	0.42	6.5	1.01
116	SMM123735621056	12 37 35.64	62 10 56.5	2.7	0.45	6.0	1.16
117	SMM123624621014	12 36 24.07	62 10 14.7	2.7	0.41	6.5	12 36 24.30	62 10 17.1	...	38	24.3	...	4.32
118	SMM123713621545	12 37 13.27	62 15 45.9	2.7	0.38	7.1	2.25
119	SMM123714621210	12 37 14.79	62 12 10.9	2.7	0.37	7.1	12 37 14.28	62 12 8.50	4.1	25	21.0	2.280 a1	2.24
120	SMM123648621116	12 36 48.78	62 11 16.0	2.6	0.34	7.8	< 12	4.29
121	SMM123739621601	12 37 39.06	62 16 1.49	2.6	0.52	5.0	12 37 39.52	62 15 58.5	...	43	23.0	...	2.31
122	SMM123653621112	12 36 53.35	62 11 12.9	2.5	0.33	7.7	12 36 53.26	62 11 16.7	...	28	19.5	0.9380 a1,k	1.98
123	SMM123637621747	12 36 37.44	62 17 47.9	2.5	0.41	6.1	1.48
124	SMM123645621845	12 36 45.76	62 18 45.0	2.5	0.46	5.4	< 12	3.68
125	SMM123613620900	12 36 13.39	62 09 0.70	2.5	0.55	4.5	< 12	2.75
126	SMM123608621251	12 36 8.737	62 12 51.5	2.5	0.44	5.5	12 36 8.671	62 12 51.0	...	39	23.0	...	2.94
127	SMM123722621835	12 37 22.92	62 18 35.7	2.5	0.55	4.5	12 37 22.53	62 18 38.2	...	30	20.2	1.524 a3	2.10
128	SMM123623621629	12 36 23.12	62 16 29.7	2.4	0.41	5.8	12 36 22.67	62 16 29.7	...	80	21.7	1.790 e	1.38
129	SMM123731621022	12 37 31.05	62 10 22.5	2.4	0.44	5.4	12 37 31.02	62 10 18.7	...	19	20.1	0.8601 a1	1.92
130	SMM123709620753	12 37 9.180	62 07 53.9	2.4	0.49	4.9	12 37 9.569	62 07 53.7	...	15	23.7	...	2.48
131	SMM123619621003	12 36 19.51	62 10 3.79	2.3	0.43	5.5	12 36 19.11	62 10 4.30	...	30	21.9	2.210 e	2.26
132	SMM123731620847	12 37 31.87	62 08 47.5	2.3	0.56	4.1	< 12	4.13
133	SMM123642621719	12 36 42.18	62 17 19.0	2.3	0.38	6.1	12 36 42.18	62 17 22.5	...	30	20.6	1.09	2.08
134	SMM123702621302	12 37 2.512	62 13 2.99	2.3	0.30	7.8	12 37 2.570	62 13 2.40	...	27	25.6	...	2.16
135	SMM123629621511	12 36 29.45	62 15 11.9	2.3	0.39	5.9	12 36 29.45	62 15 13.1	...	13	21.9	3.652 a1	4.10
136	SMM123711621243	12 37 11.09	62 12 43.9	2.3	0.34	6.6	< 12	3.46
137	SMM123655620814	12 36 55.48	62 08 14.0	2.2	0.43	5.2	< 12	0.659
138	SMM123617621407	12 36 17.72	62 14 7.70	2.2	0.40	5.6	12 36 17.83	62 14 7.91	...	51	20.4	0.8460 k	1.92
139	SMM123716621644	12 37 16.44	62 16 44.9	2.2	0.39	5.6	1.57
140	SMM123731621614	12 37 31.90	62 16 14.5	2.2	0.45	4.9	< 12	1.58
141	SMM123652621856	12 36 52.92	62 18 56.0	2.2	0.47	4.7	< 12	4.04
142	SMM123616621232	12 36 16.90	62 12 32.7	2.2	0.39	5.5	12 36 17.03	62 12 31.3	...	21	22.6	...	4.03

Table 5 continued on next page

Table 5 (*continued*)

No.	Name	R.A. (SCUBA-2) (J2000.0)	Decl. (J2000.0)	Flux (mJy)	Error (mJy)	S/N	R.A. (accurate) (J2000.0)	Decl. (J2000.0)	SMA (mJy)	20 cm (μ Jy)	K_s (AB)	z	z_{250}
(1)	(2)	(3)	(4)	(5)	(6)	(7)	(8)	(9)	(10)	(11)	(12)	(13)	(14)
143	SMM123611621033	12 36 11.35	62 10 33.5	2.1	0.47	4.5	12 36 11.52	62 10 33.5	...	26	21.4	2.40	2.25
144	SMM123618620901	12 36 18.81	62 09 1.79	2.1	0.48	4.4	12 36 18.80	62 09 0.80	...	18	22.1	1.66	2.36
145	SMM123651621457	12 36 51.92	62 14 57.9	2.1	0.32	6.7	< 12	3.99
146	SMM123607621449	12 36 7.690	62 14 49.5	2.1	0.46	4.5	12 36 7.800	62 14 49.7	...	24	22.3	2.85	3.33
147	SMM123642621545	12 36 42.90	62 15 45.0	2.1	0.35	6.0	< 12	2.26
148	SMM123706621251	12 37 6.522	62 12 51.8	2.1	0.32	6.6	< 12	3.98
149	SMM123741621253	12 37 41.40	62 12 53.4	2.1	0.47	4.4	12 37 41.40	62 12 51.0	...	167	19.8	1.598 a1	1.23
150	SMM123737621357	12 37 37.71	62 13 57.5	2.1	0.44	4.7	12 37 37.91	62 13 58.0	...	16	23.8	...	2.49
151	SMM123639621542	12 36 39.46	62 15 42.9	2.1	0.36	5.8	< 12	2.67
152	SMM123606621237	12 36 6.170	62 12 37.4	2.0	0.47	4.3	< 12	3.35
153	SMM123633620834	12 36 33.23	62 08 34.9	2.0	0.44	4.6	12 36 33.23	62 08 34.7	...	50	19.2	0.9340 b,a2	1.36
154	SMM123644621620	12 36 44.47	62 16 20.9	2.0	0.36	5.5	< 12	3.90
155	SMM123654620850	12 36 54.49	62 08 50.9	1.9	0.40	4.9	< 12	2.27
156	SMM123612621144	12 36 12.04	62 11 44.5	1.9	0.43	4.5	< 12	0.916
157	SMM123702620836	12 37 2.907	62 08 36.0	1.9	0.42	4.6	12 37 2.980	62 08 33.0	...	19	21.8	1.97	2.68
158	SMM123612621221	12 36 12.60	62 12 21.7	1.9	0.42	4.5	< 12	3.85
159	SMM123731621256	12 37 31.96	62 12 56.5	1.9	0.40	4.7	< 12	1.25
160	SMM123727621706	12 37 27.19	62 17 6.69	1.9	0.45	4.1	12 37 27.70	62 17 5.90	...	14	22.5	...	2.82
161	SMM123703621635	12 37 3.537	62 16 35.0	1.8	0.38	4.8	< 12	2.56
162	SMM123609621141	12 36 9.049	62 11 41.5	1.8	0.46	4.0	12 36 8.822	62 11 43.7	...	51	19.9	1.336 a1	1.03
163	SMM123736621240	12 37 36.53	62 12 40.5	1.8	0.43	4.2	12 37 36.80	62 12 42.7	...	30	22.1	1.67	2.09
164	SMM123649621814	12 36 49.35	62 18 14.0	1.8	0.42	4.3	12 36 49.13	62 18 13.9	...	19	21.3	2.321 a3	2.43
165	SMM123613621436	12 36 13.42	62 14 36.7	1.8	0.42	4.3	< 12	2.49
166	SMM123720621102	12 37 20.35	62 11 2.79	1.8	0.40	4.5	12 37 20.32	62 11 3.20	...	23	22.8	...	2.53
167	SMM123702621402	12 37 2.658	62 14 2.00	1.7	0.30	5.8	1.10
168	SMM123624620929	12 36 24.94	62 09 29.7	1.7	0.43	4.1	< 12	3.74
169	SMM123627621314	12 36 27.46	62 13 14.9	1.7	0.37	4.7	< 12	3.74
170	SMM123639621005	12 36 39.51	62 10 5.00	1.7	0.40	4.3	< 12	1.54
171	SMM123724621629	12 37 24.03	62 16 29.7	1.7	0.41	4.2	< 12	3.71
172	SMM123710621429	12 37 10.96	62 14 29.9	1.7	0.35	4.8	< 12	3.70
173	SMM123706621607	12 37 6.690	62 16 7.90	1.7	0.37	4.5	< 12	1.81
174	SMM123655621023	12 36 55.21	62 10 23.9	1.6	0.36	4.6	< 12	3.67
175	SMM123713621143	12 37 13.37	62 11 43.9	1.6	0.38	4.3	12 37 13.17	62 11 45.5	...	20	23.0	2.413 a3	3.29
176	SMM123648621214	12 36 48.78	62 12 14.9	1.6	0.30	5.5	12 36 48.65	62 12 15.7	...	22	20.9	1.066 a1	1.85
177	SMM123620621110	12 36 20.64	62 11 10.7	1.6	0.40	4.0	12 36 20.98	62 11 13.7	...	19	20.1	0.9447 a1	1.33
178	SMM123713621251	12 37 13.67	62 12 51.8	1.6	0.35	4.5	12 37 13.69	62 12 49.4	...	12	22.5	0.8992 a1	3.63
179	SMM123657621654	12 36 57.52	62 16 54.9	1.5	0.38	4.1	< 12	3.59
180	SMM123707621127	12 37 7.928	62 11 27.9	1.5	0.36	4.3	< 12	1.80
181	SMM123701621513	12 37 1.237	62 15 13.9	1.5	0.34	4.5	< 12	2.17
182	SMM123645621148	12 36 45.35	62 11 48.0	1.5	0.32	4.6	< 12	2.73
183	SMM123657621407	12 36 57.51	62 14 7.00	1.4	0.29	5.0	12 36 57.37	62 14 7.99	...	28	21.0	1.462 a1,a3	1.63
184	SMM123706621156	12 37 6.372	62 11 56.0	1.4	0.34	4.2	12 37 5.859	62 11 53.6	...	44	19.1	0.9015 a1,a3	1.06
185	SMM123634621215	12 36 34.92	62 12 15.9	1.4	0.35	4.000891
186	SMM123656621254	12 36 56.07	62 12 54.0	1.4	0.28	4.9	< 12	3.44

Table 5 continued on next page

Table 5 (*continued*)

No.	Name	R.A.	Decl.	Flux	Error	S/N	R.A.	Decl.	SMA	20 cm	K_s	z	z_{250}
		(SCUBA-2)					(accurate)						
		(J2000.0)	(J2000.0)	(mJy)	(mJy)		(J2000.0)	(J2000.0)	(mJy)	(μ Jy)	(AB)		
(1)	(2)	(3)	(4)	(5)	(6)	(7)	(8)	(9)	(10)	(11)	(12)	(13)	(14)

^{a1}Our DEIMOS redshift^{a2}Our LRIS redshift^{a3}Our MOSFIRE redshift^bWirth et al. 2004^cChapman et al. 2005^dSwinbank et al. 2004^ePope et al. 2008^{f1}Daddi et al. 2009b^{f2}Daddi et al. 2009a^gBothwell et al. 2013^hWalter et al. 2012^kCohen et al. 2000Table 6. SCUBA-2 450 Micron Sample (4σ)

No.	Name	R.A.	Decl.	450 μ m		S/N	R.A. (accurate)	Decl.	SMA	20 cm	K_s	z	850 μ m
				Flux	Error								Flux
		(J2000.0)	(J2000.0)	(mJy)	(mJy)		(J2000.0)	(J2000.0)	(mJy)	(μ Jy)	(AB)		(mJy)
(1)	(2)	(3)	(4)	(5)	(6)	(7)	(8)	(9)	(10)	(11)	(12)	(13)	(14)
1	SMM123730621259	12 37 30.69	62 12 59.6	42	4.1	10.	12 37 30.80	62 12 58.7	14.9	123	22.9	2.43	13.
2	SMM123553621335	12 35 53.70	62 13 35.1	39	9.5	4.1	12 35 53.86	62 13 37.2	...	32	19.6	0.8810	5.9
3	SMM123721620709	12 37 21.01	62 07 9.79	35	6.9	5.0	12 37 21.40	62 07 8.30	...	293	20.9	...	6.4
4	SMM123741621222	12 37 41.40	62 12 22.4	33	5.3	6.3	12 37 41.16	62 12 21.0	7.10	28	23.3	3.02	5.4
5	SMM123618621549	12 36 18.84	62 15 49.7	30	4.4	6.9	12 36 18.35	62 15 50.4	7.20	169	22.0	2.000	6.4
6	SMM123634621918	12 36 34.71	62 19 18.9	30	6.8	4.4	< 12	5.3
7	SMM123629621045	12 36 29.21	62 10 45.8	28	3.9	7.2	12 36 29.03	62 10 45.5	7.70	91	19.7	1.013	4.3
8	SMM123711621328	12 37 11.39	62 13 28.9	28	3.3	8.4	12 37 11.34	62 13 30.9	6.70	126	20.4	1.995	8.1
9	SMM123701621146	12 37 1.651	62 11 46.9	26	3.0	8.7	12 37 1.578	62 11 46.4	4.80	95	20.5	1.760	6.3
10	SMM123707621407	12 37 7.236	62 14 7.91	26	3.2	8.0	12 37 7.177	62 14 8.19	7.10	28	21.4	2.45	8.0
11	SMM123616621513	12 36 16.42	62 15 13.7	24	4.3	5.5	12 36 16.10	62 15 13.7	3.40	38	22.2	2.578	4.6
12	SMM123726620823	12 37 26.16	62 08 23.7	23	5.4	4.3	12 37 26.66	62 08 23.2	...	51	21.2	2.59	4.3
13	SMM123635621423	12 36 35.76	62 14 23.9	22	3.5	6.2	12 36 35.59	62 14 24.0	...	78	20.1	2.005	3.8
14	SMM123622621629	12 36 22.70	62 16 29.7	22	4.5	4.9	12 36 22.67	62 16 29.7	...	81	21.7	1.790	3.9
15	SMM123622621616	12 36 22.26	62 16 16.7	21	4.4	4.8	12 36 22.10	62 16 15.9	5.40	20	23.9	...	4.6
16	SMM123634621239	12 36 34.90	62 12 39.9	20	3.3	6.0	12 36 34.51	62 12 40.9	...	188	19.9	1.224	2.5
17	SMM123716621640	12 37 16.14	62 16 40.9	20	4.2	4.7	< 12	1.9
18	SMM123646621448	12 36 46.05	62 14 48.9	19	3.2	5.9	12 36 46.08	62 14 48.6	4.20	103	22.4	3.63	5.9
19	SMM123642621721	12 36 42.18	62 17 21.9	18	4.0	4.5	12 36 42.18	62 17 22.5	...	24	20.6	...	2.2
20	SMM123646620833	12 36 46.65	62 08 33.9	18	3.9	4.6	12 36 46.68	62 08 33.2	...	95	19.0	0.9710	2.5
21	SMM123631621714	12 36 31.99	62 17 14.9	17	4.3	4.0	12 36 31.94	62 17 14.7	7.10	22	23.0	...	8.4
22	SMM123726621328	12 37 26.12	62 13 28.7	17	3.9	4.5	< 12	0.28
23	SMM123637620854	12 36 37.08	62 08 54.0	17	4.0	4.3	12 36 37.03	62 08 52.4	...	90	22.0	2.13	4.3

Table 6 continued on next page

Table 6 (*continued*)

No.	Name	R.A.	Decl.	450 μ m		S/N	R.A. (accurate)	Decl.	SMA	20 cm	K_s	z	850 μ m Flux
				Flux	Error								
		(J2000.0)	(J2000.0)	(mJy)	(mJy)		(J2000.0)	(J2000.0)	(mJy)	(μ Jy)	(AB)		(mJy)
(1)	(2)	(3)	(4)	(5)	(6)	(7)	(8)	(9)	(10)	(11)	(12)	(13)	(14)
24	SMM123631620957	12 36 31.51	62 09 57.9	16	3.9	4.1	12 36 31.26	62 09 57.6	...	140	21.7	2.313	2.9
25	SMM123713621153	12 37 13.79	62 11 53.9	16	3.6	4.4	12 37 14.05	62 11 56.5	3.20	21	24.2	...	2.5
26	SMM123628621313	12 36 28.17	62 13 13.8	16	3.6	4.4	< 12	1.4
27	SMM123633621408	12 36 33.46	62 14 8.89	15	3.6	4.2	12 36 33.42	62 14 8.50	12.0	33	25.5	4.042	9.2
28	SMM123700620911	12 37 0.487	62 09 11.0	15	3.8	4.0	12 37 0.270	62 09 9.70	3.10	297	21.8	...	2.0
29	SMM123712621325	12 37 12.53	62 13 25.9	14	3.4	4.1	< 12	3.2
30	SMM123651621228	12 36 51.92	62 12 28.0	13	2.7	4.7	12 36 52.03	62 12 25.9	7.80	12	99.0	5.183	5.6
31	SMM123652621355	12 36 52.35	62 13 55.0	11	2.8	4.1	12 36 52.78	62 13 54.3	...	21	21.1	1.355	0.58

Table 7. Comparison with Previous Wide-field mm/submm Surveys

Name	Present (850 μ m) (mJy)	S2CLS 850 μ m) (mJy)	Wang:SCUBA (850 μ m)	Pope:SCUBA (850 μ m) (mJy)	AzTEC+MAMBO (1.16 mm) (mJy)	GISMO (2 mm)
(1)	(2)	(3)	(4)	(5)	(6)	(7)
2 SMM123712622210	17.3 (0.94)	20.3 (2.1)	10.2 (0.68)	...
3 SMM123730621258	13.4 (0.39)	12.8 (0.97)	13.6 (2.2)	...	4.51 (0.55)	...
7 SMM123627620605	11.2 (0.80)	10.6 (1.6)	4.81 (0.67)	...
8 SMM123633621407	9.44 (0.36)	8.37 (0.90)	12.9 (2.1)	11.3 (1.6)	5.24 (0.57)	0.790 (0.14)
12 SMM123550621041	8.69 (0.80)	11.5 (1.4)	5.00 (0.71)	...
13 SMM123711621329	8.58 (0.34)	9.69 (0.90)	4.40 (1.3)	...	4.09 (0.54)	...
14 SMM123631621712	8.46 (0.40)	7.28 (0.97)	4.22 (0.56)	...
15 SMM123707621408	8.34 (0.33)	7.09 (0.89)	...	10.7 (2.7)
18 SMM123618621549	7.35 (0.42)	7.62 (0.99)	7.72 (1.0)	7.50 (0.90)
20 SMM123634621921	6.91 (0.70)	5.48 (1.1)	2.44 (0.61)	...
21 SMM123721620709	6.74 (0.74)	5.70 (1.3)
22 SMM123722620539	6.74 (0.87)	8.53 (1.6)
24 SMM123644621938	6.61 (0.69)	6.62 (1.0)	3.03 (0.59)	...
25 SMM123701621145	6.56 (0.32)	6.71 (0.86)	...	3.90 (0.70)
26 SMM123652621224	6.30 (0.29)	5.97 (0.83)	5.12 (0.47)	5.90 (0.30)	...	0.420 (0.13)
27 SMM123539621241	6.22 (0.88)	2.97 (0.75)	...
28 SMM123812621453	6.18 (0.97)	2.78 (0.73)	...
29 SMM123632620621	6.08 (0.76)	3.31 (0.66)	...
31 SMM123646621447	5.99 (0.32)	6.74 (0.92)	10.8 (2.2)	8.60 (1.4)
32 SMM123616620701	5.97 (0.77)	7.08 (1.5)
34 SMM123714621824	5.93 (0.46)	4.65 (1.0)	3.46 (0.57)	...
35 SMM123741621221	5.86 (0.47)	7.92 (1.0)	2.41 (0.57)	...
36 SMM123610620646	5.81 (0.84)	7.52 (1.7)
38 SMM123738621731	5.61 (0.71)	2.62 (0.58)	...
40 SMM123648622104	5.57 (0.79)	7.18 (1.2)	3.05 (0.63)	...
42 SMM123622621620	5.42 (0.41)	6.15 (0.98)	10.2 (1.2)
43 SMM123616621514	5.42 (0.42)	5.99 (0.99)	6.20 (1.0)	...	2.61 (0.55)	...
45 SMM123636620708	5.34 (0.56)	3.35 (0.61)	...
49 SMM123635621424	4.97 (0.35)	5.20 (0.91)

Table 7 continued on next page

Table 7 (*continued*)

Name	Present (850 μ m) (mJy)	S2CLS 850 μ m (mJy)	Wang:SCUBA (850 μ m)	Pope:SCUBA (850 μ m) (mJy)	AzTEC+MAMBO (1.16 mm) (mJy)	GISMO (2 mm)
(1)	(2)	(3)	(4)	(5)	(6)	(7)
51 SMM123621621706	4.94 (0.44)	4.95 (1.0)	8.69 (1.9)	8.90 (1.5)
52 SMM123651620500	4.85 (0.86)	6.76 (1.6)	3.74 (0.88)	...
53 SMM123712621035	4.84 (0.39)	4.38 (0.94)
55 SMM123627621218	4.82 (0.37)	7.09 (0.97)	2.61 (0.57)	...
57 SMM123719621218	4.69 (0.38)	3.98 (0.92)
58 SMM123743620752	4.66 (0.83)	5.79 (1.5)
62 SMM123637620853	4.44 (0.42)	3.54 (1.0)
63 SMM123629621045	4.44 (0.40)	...	5.72 (1.3)
64 SMM123636621156	4.43 (0.35)	3.67 (0.90)	...	7.00 (0.90)
65 SMM123658620932	4.42 (0.38)	5.20 (0.99)
73 SMM123702621426	4.09 (0.31)	3.51 (0.88)
75 SMM123728621920	4.07 (0.75)	4.35 (1.1)
77 SMM123712621211	4.04 (0.36)	4.75 (0.88)	2.59 (0.55)	...
78 SMM123658621451	3.99 (0.32)	3.82 (0.89)
80 SMM123656621205	3.97 (0.30)	4.00 (0.84)
82 SMM123605620836	3.87 (0.75)	4.95 (1.4)
86 SMM123634620940	3.65 (0.41)	3.43 (0.96)	4.23 (1.3)
91 SMM123609620800	3.57 (0.76)	6.04 (1.4)
95 SMM123719621021	3.50 (0.41)	3.97 (0.95)
98 SMM123608620852	3.39 (0.72)	2.42 (0.60)	...
102 SMM123713621156	3.24 (0.38)	3.64 (0.89)
105 SMM123717620801	3.16 (0.51)	3.97 (1.1)	2.74 (0.67)	...
110 SMM123634621239	2.92 (0.34)	3.57 (0.90)
112 SMM123700620910	2.85 (0.39)	9.00 (2.1)
115 SMM123646620833	2.76 (0.42)	4.04 (1.0)
126 SMM123608621251	2.50 (0.44)	16.8 (4.0)
128 SMM123623621629	2.45 (0.41)	3.55 (0.99)
131 SMM123619621003	2.39 (0.43)	...	6.01 (1.7)	6.70 (1.6)
134 SMM123702621302	2.36 (0.30)	3.20 (0.60)
141 SMM123652621856	2.23 (0.47)	3.91 (1.0)
143 SMM123611621033	2.19 (0.47)	4.41 (1.0)
158 SMM123612621221	1.94 (0.42)	...	3.75 (1.1)
166 SMM123720621102	1.83 (0.40)	4.11 (0.92)